Coordination Chemistry Reviews 474 (2023) 214846

Contents lists available at ScienceDirect

Coordination Chemistry Reviews

journal homepage: www.elsevier.com/locate/ccr

Review

Recent progress in the applications of non-metal modified graphitic carbon nitride in photocatalysis

Chensi Tang [a,b], Min Cheng [a,b,*], Cui Lai [a,b,*], Ling Li [a,b], Xiaofeng Yang [a,b], Li Du [a,b], Gaoxia Zhang [a,b], Guangfu Wang [a,b], Lu Yang [a,b]

[a] College of Environmental Science and Engineering, Hunan University, Changsha, Hunan 410082, China
[b] Key Laboratory of Environmental Biology and Pollution Control (Hunan University), Ministry of Education, Changsha, Hunan 410082, China

ARTICLE INFO

Article history:
Received 24 April 2022
Accepted 11 September 2022

Keywords:
G-C_3N_4
Non-metal modification
Photocatalysts
Applications

ABSTRACT

Over the past few decades, graphitic carbon nitride (g-C_3N_4) has gained increasing interest due to its unique and excellent properties. To improve its inherent drawbacks and perfect its catalytic performance, many convenient and facile strategies have been developed, including metal and non-metal modifications. However, the low content in nature and the leaching of toxic metals in photocorrosion have been two critical obstacles for metal-based photocatalysts in practical applications. Therefore, it is increasingly urgent to develop and design efficient and stable non-metal modified g-C_3N_4-based photocatalysts. Here, this review begins with a brief presentation of the unique characteristics of g-C_3N_4. Then, to maintain the metal-free nature of g-C_3N_4, the four most frequently used modification strategies are discussed, including vacancies introduction, doping with non-metal elements, modifying with non-metal quantum dots and coupling with other semiconductors. In addition, the latest developments of non-metal modified g-C_3N_4-based photocatalysts for energy-related and environmental applications are systematically discussed. In the end, both the current development bottlenecks and future development directions of g-C_3N_4-based metal-free photocatalysts are presented. Basically, we highlight the unique properties of completely non-metal modified g-C_3N_4, which has positive implications for the sustainable development of g-C_3N_4-based non-metal photocatalysts. Furthermore, we hope that it can spark new ideas and present promising directions to design metal-free photocatalysts for energy-related and environmental applications.

Contents

* Corresponding authors at: College of Environmental Science and Engineering, Hunan University, Changsha, Hunan 410082, China.
E-mail addresses: chengmin@hnu.edu.cn (M. Cheng), laicui@hnu.edu.cn (C. Lai).

https://doi.org/10.1016/j.ccr.2022.214846
0010-8545/

1. Introduction

Due to the process of economic development since the 20th century, the negative effects of the highly developed industry are not anticipated enough and the prevention is not in place, resulting in a global energy crisis and environmental pollution [1,2]. Fortunately, numerous innovative exploration and frontlines have demonstrated that semiconductor photocatalysis technology may be one of the most prospective strategies to combat above two serious problems [3–6]. Then, g-C_3N_4 has gradually entered the limelight as a typical visible light reactive semiconductor. What is noteworthy is that it possesses numerous eminent properties, such as high degree of thermal and chemical stability, various cheap nitrogen-rich precursors, relatively narrow bandgap (2.7 eV) and environmental friendliness, making it frequently used for environmental and energy applications [7,8]. Zhu et al. comprehensively summarized the synthetic methods for synthesizing g-C_3N_4 with different structures and morphologies, and reviewed the applications of g-C_3N_4 in various heterogeneous catalysis [9]. Among these, the most common applications are hydrogen (H_2) production and wastewater treatment. There are many preeminent reviews described the characters of g-C_3N_4-based photocatalysts in these fields [10,11]. For example, Naseri [12] summarized the fundamental concepts and principles of photocatalytic H_2 production. Very recently, Ritu Malik reviewed the recent progress of continuous H_2 production by different nanostructures and morphologies of g-C_3N_4 with special attention to modified high surface area g-C_3N_4 [13]. Wang et al. presented in great detail the effects of different modification strategies on the physical and chemical properties of g-C_3N_4, including elemental doping, copolymerization, crystalline tailoring, surface engineering, single-atom modification, dimension controlling and heterojunctions construction. In particular, the focus was on exploring the catalytic mechanism of these modified g-C_3N_4 composites in H_2 production by photocatalytic water splitting [14]. Besides, Cui et al. [15] highlighted the advances of g-C_3N_4-based membranes for water purification. Dharm Pal et al. [16] summarized the recent developments in the photodegradation of antibiotics by metal and non-metal elements doped g-C_3N_4-based photocatalysts. Many excellent studies have been done on g-C_3N_4 for H_2 production and pollutants removal, thus, we will not repeat here.

Unfortunately, there are some non-negligible issues that severely limit the catalytic property of g-C_3N_4, for instance, small specific surface area (SSA), the rapid recombination of photoexcited electron–hole (photoexcited e^-/h^+) pairs, unsatisfactory visible light response range and so on [17–20]. In an attempt to address these limitations, some researchers (including our team [21–25]) have figured out many effective and feasible strategies, including designing nanostructure (template and template-free synthesis approaches, exfoliation, self-assembly) [26–30], modifying electron redistribution (metal, non-metal elements- and co-doping) [31–33] and coupling with other substances (metal or non-metal materials) [34–36]. Thankfully, numerous results have shown that the catalytic performance of g-C_3N_4 could indeed be conveniently improved through the above channels. A large number of important and interesting researches have revealed that metal-containing g-C_3N_4-based materials possessed significantly enhanced catalytic properties. There are also many excellent review articles in this field. For example, Lin et al. minutely summarized the construction of direct or indirect Z-scheme heterojunctions by coupling with other metal-containing semiconductors to significantly improve the performance of g-C_3N_4 in photocatalytic CO_2 reduction [37]. However, expensive raw materials, poor chemical durability, toxic metal-leaching from photo-corrosion and deficiency in nature seriously hindered the large-scale applications of metal-based photocatalysts [38,39]. Development to this point, exploring and designing of efficient and stable non-metal-based photocatalysts as candidates was a feasible solution due to their much impressive properties as observed in lots of photocatalytic reactions. In the past few years, significant progress has also been made in this area, and the results showed that some non-metal photocatalysts exhibited comparable or even better performance than metal-based photocatalysts, which made them highly promising for applications without the drawbacks of metal-based photocatalysts. But the superior metal-free properties have not received nearly enough importance, with only a few retrospective investigations focusing on presenting the performance of non-metal modified g-C_3N_4. For example, Zhou et al. [39] summarized different metal-based photocatalysts first, and then, the effect of non-metal modification means on the structures and properties of g-C_3N_4, but this article did not investigate the applications of modified g-C_3N_4 in different aspects. Zhang et al. [40] summarized the effects of doping with metal and non-metal elements on the properties of g-C_3N_4 using characterization techniques. In addition, He et al. [41] reviewed the influences of non-metal modification on the composition and morphology of g-C_3N_4, and mainly mentioned their photocatalytic applications in H_2 production, water treatment and CO_2 reduction. However, recent studies have found that g-C_3N_4-based metal-free photocatalysts also had promising applications in nitrogen oxides (NO_x) purification, hydrogen peroxide (H_2O_2) production and bacterial disinfection. Therefore, it is timely to conduct a comprehensive review that focuses completely on the properties of non-metal modified g-C_3N_4 and their performance in aforementioned applications.

Based on this, in this work, a critical overview of the up-to-date progress in the applications of non-metal modified g-C_3N_4 photocatalysts is provided. To maintain the metal-free nature of g-C_3N_4, we discuss four frequently used modification methods. Firstly, we introduce the unique characteristics of g-C_3N_4 and different non-metal modification strategies. Then, the recent developments of g-C_3N_4-based metal-free photocatalysts for energy-related and environmental applications will be systematically discussed. Finally, we present the current development bottlenecks and future development directions of g-C_3N_4-based metal-free photocatalysts.

2. Characteristics of g-C_3N_4

As we all know, g-C_3N_4 was a novel polymer semiconductor, in which C and N atoms were hybridized in sp^2 to make up a delocalized π-conjugated system. It was found that g-C_3N_4 had two basic tectonic units, the triazine ring (Fig. 1A) and 3-s-triazine ring (Fig. 1B), which extended indefinitely to constitute a mesh

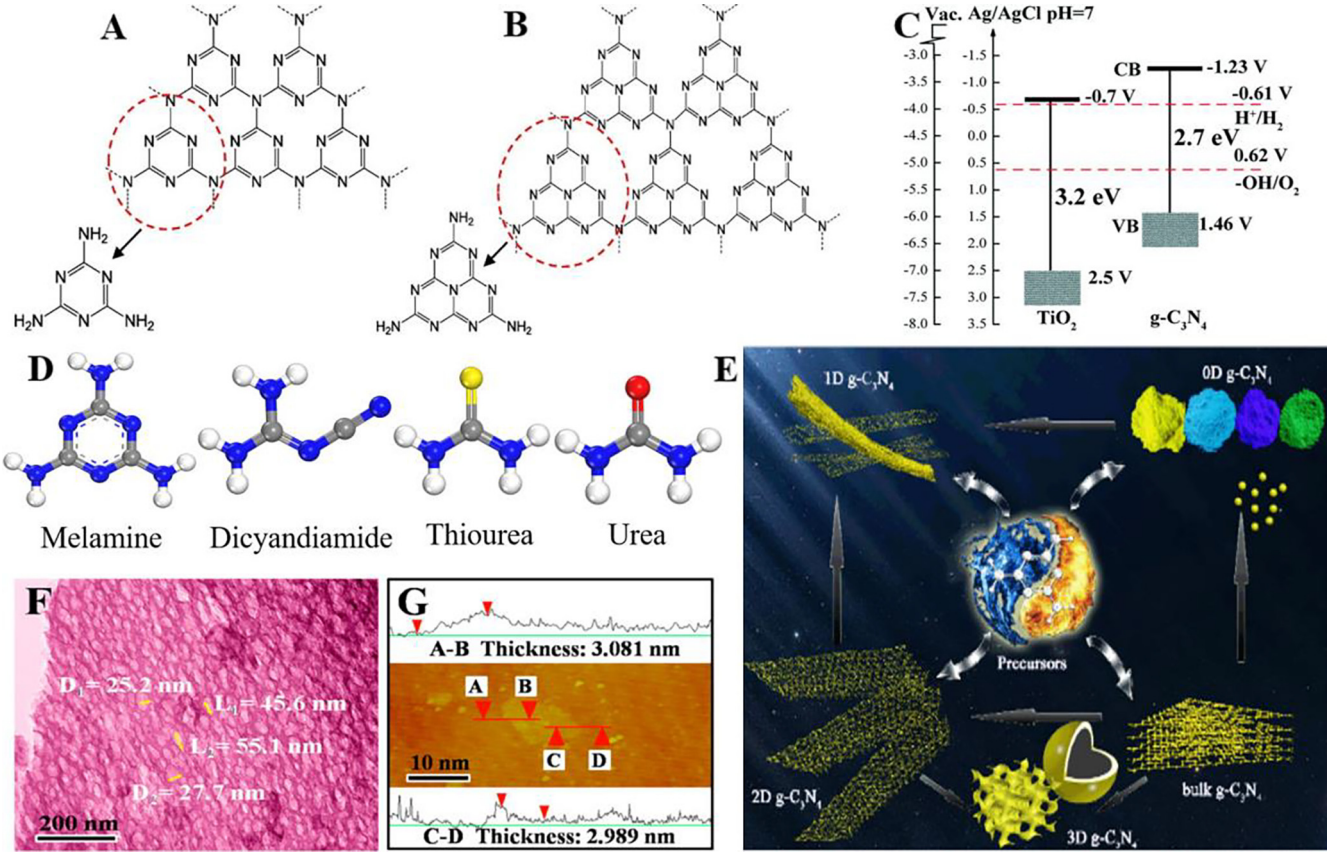

Fig. 1. (A) Triazine and (B) 3-s-triazine structures of g-C_3N_4. Reproduced with permission from ref. [42]. Copyright 2016, American Chemical Society. (C) Electronic band structure of g-C_3N_4, compared with the well-known inorganic photocatalyst, titanium dioxide (TiO_2). Reproduced with permission from ref. [52]. Copyright 2018, Royal Society of Chemistry. (D) The chemical structures of common g-C_3N_4 precursors. The gray, blue, white, yellow, and red spheres represent C, N, H, S and O atoms, respectively. (E) Schematic diagram of the transitions among bulk, 0D, 1D, 2D and 3D g-C_3N_4. Reproduced with permission from ref. [49]. Copyright 2019, Springer Nature. (F) TEM image of UM3. (G) AFM image and the height distribution profiles of separated layer from UM3. Reproduced with permission from ref. [51]. Copyright 2018, American Chemical Society. (For interpretation of the references to color in this figure legend, the reader is referred to the web version of this article.)

structure [42]. And between them, the 3-s-triazine ring that connected to form g-C_3N_4 was more stable, which has been subtly confirmed by DFT calculations [43]. The N p_z orbitals formed the highest occupied molecular orbitals (HOMO), while the C p_z orbitals formed the lowest unoccupied molecular orbitals (LUMO) of g-C_3N_4. In other words, the valence bands (VB) and conduction bands (CB) are mainly determined by N p_z orbitals and C p_z orbitals, respectively. The g-C_3N_4 had a mild bandgap (~2.7 eV) (Fig. 1C), which allowed it to harvest visible light in the solar spectrum at wavelengths less than 460 nm [8,44].

Pure g-C_3N_4 is typically synthesized by calcining nitrogen-rich precursors at temperatures between 450 and 650 °C for 2–4 h. The most frequent precursors of pristine g-C_3N_4 are dicyandiamide, melamine, urea, thiourea and their chemical structures are shown in Fig. 1D. In the meantime, since different precursors contained different foreign chemical elements (sulfur or oxygen), different polymerization reactions occurred during the forming process of g-C_3N_4, which had a powerful impact on the character of the eventually formed g-C_3N_4 [45]. With this specific focus, Zou et al. [46] systematically investigated the morphologies and microstructures of g-C_3N_4 synthesized via calcining different precursors (dicyandiamide, melamine, and urea) under identical conditions. The results showed that g-C_3N_4 synthesized with urea as precursor tended to form porous thin nanosheets structure, while g-C_3N_4 synthesized with melamine and dicyandiamide as precursors tended to form thick layered structure. Certainly, precursors containing different heteroatoms strongly influenced the morphological framework and SSA, and thus affected the photocatalytic performance of the synthesized g-C_3N_4, since a larger SSA usually meant more reactive sites could be exposed. For instance, Wang and his colleagues induced nanoropes-like structure inside of g-C_3N_4 using naphthalene [47], which could be easily recycled on industrial scale. Due to the violent movement of the naphthalene molecular vapor at higher temperatures, the modified g-C_3N_4 had a larger SSA than bulk g-C_3N_4 (351.08 m^2/g vs 15.82 m^2/g). Wang et al. [48] successfully prepared porous g-C_3N_4 by the co-polymerization of acidified melamine and urea. Pre-acidification of melamine weakened the g-C_3N_4 interlayer forces, which facilitated the growth of g-C_3N_4 sheets. And urea can be decomposed into CO_2 and H_2O, which can promote the formation of porous structures. These strategies gave the as-prepared composites an in-plane porous structure and an enormous SSA, which exposed more accessible active sites and made the photocatalytic performance much better.

On the other hand, controlling the dimension was also a frequent scene for tuning the characteristics of g-C_3N_4. Fig. 1E showed the schematic diagram of g-C_3N_4 in different dimensions, including bulk, 0D, 1D, 2D and 3D g-C_3N_4, and the transition processes among them. 0D g-C_3N_4 usually meant g-C_3N_4 dots, which possessed quantum effects. The morphology of 1D g-C_3N_4 included nanotube, nanorod and nanowire. Among them, g-C_3N_4 nanotubes were widely studied because the tubular structure can excite additional excellent properties [14]. In general, 0D and 1D g-C_3N_4 could be manufactured via altering the arrangement and number of 3-s-triazine rings. 2D g-C_3N_4 mainly meant g-C_3N_4 nanosheets,

Table 1
Effects of different non-metal element doping on the properties of g-C_3N_4.

Dopant (s)	Catalyst	Synthetic method	Bandgap (eV) (pour vs doping)	SSA (m^2/g) (pour vs doping)	Application	Improved performance	Reusability and stability (after 5 cycles)	Ref.
C	BTPMC g-C_3N_4	thermal condensation	2.75 vs 2.28	48.6 vs 49.6	photocatalytic BPA degradation	–	no significant change	[79]
N	NDCN-4S	thermal treatment	2.51 vs 2.54	18.36 vs 74.79	photocatalytic TC degradation	2.07 times	slightly decreased	[68]
N	TCN(NH_3)	supramolecular self-assembly	–	8.6 vs 135.8	photocatalytic CO_2 reduction	17 times	maintained at 100 μmol g^{-1} h^{-1}	[80]
B	B/g-C_3N_4	ionic liquid assistance	3.16 vs 2.22	10.28 vs11.41	photocatalytic H_2 production	3 times	remained unchanged after 3rd	[81]
B	BCN	thermal treatment	2.76 vs 2.50	48 vs 123	photocatalytic N_2 reduction	nearly 10 times	basically unchanged	[60]
O	40 % OA-g-C_3N_4	condensation	2.91 vs 2.08	35.3 vs 105.2	photocatalytic BPA degradation	4.7 times	decreased from 100 % to 93 %	[63]
O	O-CN	thermal polymerization	–	54.77 vs 127.89	organic pollutants degradation	–	decreased from 100 % to 94 % (BPA)	[62]
S	MTCN-6	self-assembling	2.71 vs 2.64	16.3 vs 66.4	photocatalytic H_2 generation	11 times	no obvious decrease	[82]
P	P-C_3N_4	thermal co-poly-condensation	2.67 vs 2.57	12.37 vs 40.89	photocatalytic Rh B degradation	18 times	decreased from 100 % to 91.2 %	[83]
P	CN-SP	hydrothermal method	2.75 vs 2.63	8.6 vs 28.2	photocatalytic H_2 generation	–	–	[84]
F	CNF-0.5	hydrothermal method	2.69 vs 2.63	–	photocatalytic H_2 generation	2.7 times	without losing of activity after 4th	[85]
Cl	CN-Cl_x	thermal polycondensation	2.61 vs 2.72	–	OER and photodegradation Rh B	4 times (degradation)	–	[86]
Br	CN–Br20	thermal polymerization	2.8 vs 2.74	9.086 vs 13.397	photoreduction Cr(VI)	2.0 times	maintained at 50 %	[87]
Br	CNU-$Br_{0.1}$	one-pot co-condensation	2.86 vs 2.79	- vs 54	photocatalytic water splitting	–	no activity decreased after 4th	[88]
I	g-C_3N_4-GLC-NH_4I	dynamic gaseous templates method	2.72 vs 2.50	16.53 vs 81.52	photocatalytic H_2 evolution	6.5 times	no significant reduction after 4th	[89]
I	IGCNSs	*in situ* ball-milling technique	2.59 vs 2.37	10.0 vs 80.2	photocatalytic water splitting	nine-folds	high stability after 3rd	[90]
Si	CNSi	thermal treatment	2.77 vs 2.75	39.7 vs 42.4	photocatalytic H_2 production and Rh B degradation	2.7 and 2.5 times	no obvious decrease after 4th	[77]
B-P	BPCNNS	thermal etching route	2.65 vs 2.61	8.4 vs 85.6	photodegradation OTC and Rh B	2.9 and 5.9 times	no evident decrease	[71]
P—S	PSCN-50	*in situ* thermal copolymerization	2.70 vs 2.62	6.42 vs 25.87	photodegradation TC and MO	3.7 and 6.0 times	from 85.85 % to 80.52 % and 73.25 % to 68.78 %	[91]
C—O	$OCCN_{0.25}$	thermal condensation	2.74 vs 2.03	11.43 vs 18.26	photocatalytic CO_2 reduction	4.3-fold	remain stable after 4th	[92]
P-Cl	ClPCN-2	co-pyrolysis	2.68 vs 2.73	32.68 vs 41.78	photodegradation Rh B and NOR	5.9 and 2.0 times	no dramatic decrease after 4 cycles (Rh B)	[93]
O—S	HGCNOS	hydrothermal method	2.68 vs 2.77	14.84 vs 13.62	photocatalytic N_2 fixation	4.1 times	no significant decrease	[94]
S-B	SBCN	thermal treatment	2.70 vs 2.48	–	photocatalytic Rh B degradation	6.5 times	no obvious decrease	[70]
P—O	P—O—C_3N_4	hydrothermal method	2.68 vs 2.51	12.8 vs 92.5	photocatalytic Rh B degradation	27 times	no obvious difference after 3rd	[95]
C-I	$CNIN_{0.2}$	post-thermal treat and co-polymerization	2.75 vs 2.81	14.6 vs 54.4	photocatalytic H_2 evolution	9.8 times	slight change after 4th	[96]
S—P—O	CN-SPO	annealing method	2.4 vs 2.34	12.3 vs 23.2	photocatalytic H_2 evolution	5 times	–	[75]

and a facile strategy to get it was exfoliation of bulk g-C_3N_4, including thermal exfoliation, acid and alkaline exfoliation [49]. For instance, Li and his colleagues [50] prepared macroscopic foam-like porous ultra-thin g-C_3N_4 nanosheets with abundant pores of various sizes by thermal oxidation exfoliation of bulk g-C_3N_4 in an air atmosphere. The SSA of calculated g-C_3N_4 nanosheets was up to 277.98 m^2/g, 26-fold higher than that of calculated bulk g-C_3N_4 (10.89 m^2/g). In addition, 3D spherical g-C_3N_4 could be composed of several layers of nanosheets. In 2017, Zhang and his co-workers subjected melamine in aqueous urea for hydrothermal treatment prior to the calcination step [51]. The obtained original precursor could be ultimately calcined to be 3D ultra-thin porous N self-doped g-C_3N_4 (UM3) after subsequent treatment. The TEM image (Fig. 1F) showed a mesopore size distribution around 25 × 50 nm, and AFM image (Fig. 1G) showed a height of about ~ 3.0 nm, which contained approximately 7 or 8 layers of g-C_3N_4 sheets. In brief, the morphological structures and optical characteristics of g-C_3N_4 could be controlled on the basis of the synthesis conditions, which had inspired an increasing number of modifications later.

3. g-C_3N_4-based metal-free photocatalysts

As we all know, semiconductor-mediated photocatalysis technology mainly involves the following four consecutive steps: (1) harvest of light, (2) generation of photoexcited e^-/h^+ pairs, (3) separation and migration of photoexcited e^-/h^+ pairs, and (4) surface adsorption and redox reactions [53]. Admittedly, g-C_3N_4-mediated photocatalysis technology is no exception. When exposed to light with energy equal to or greater than the bandgap energy of g-C_3N_4, electrons can be excited from the VB to CB, and a

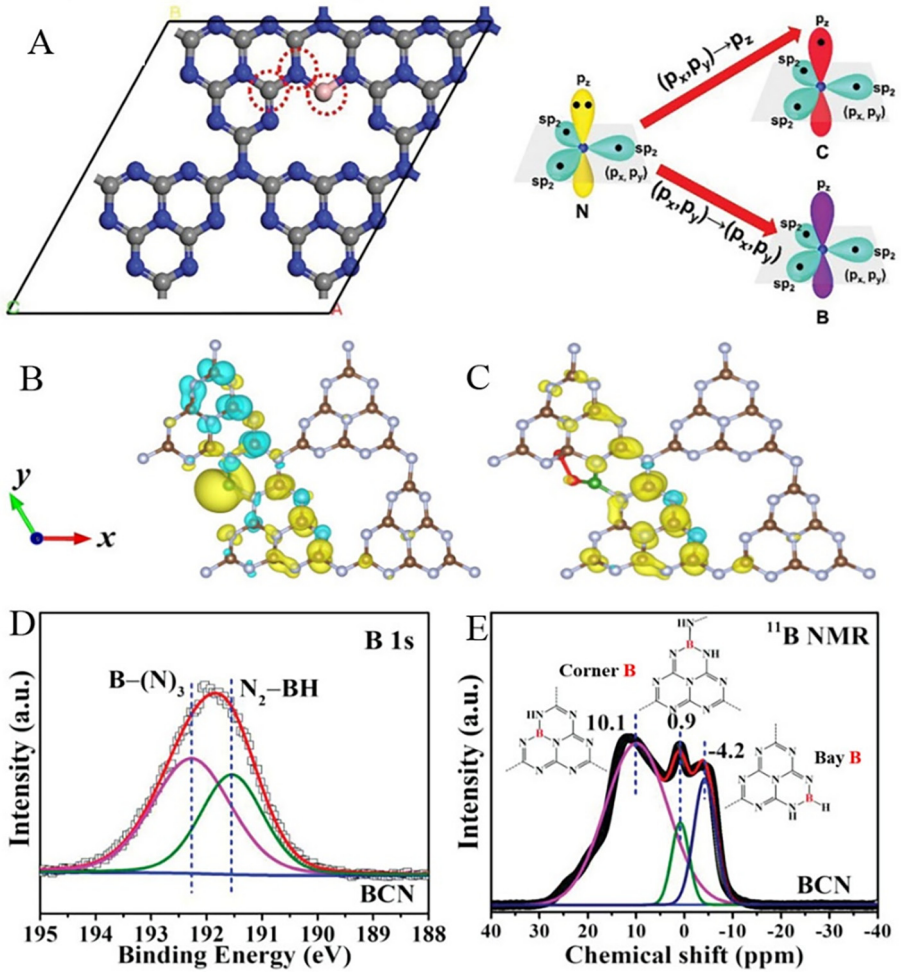

Fig. 2. (A) Schematic diagram of electrons excited from N ($2p_x$, $2p_y$) to C $2p_z$ or B ($2p_x$, $2p_y$). The gray, blue and pink balls represent the C, N and B atoms, respectively. Reproduced with permission from ref. [58]. Copyright 2019, Wiley-VCH. (B) Spin-resolved charge density of BCN and (C) its most possible O_2 adsorption configurations modeled by supercells. The isosurface value is set to be 0.002 electron/Å^3, and the positive and negative densities are shown in yellow and cyan, respectively. Reproduced with permission from ref. [59]. Copyright 2020, American Chemical Society. (D) High-resolution B 1 s spectra and (E) ^{11}B solid state nuclear magnetic resonance spectra of BCN. Reproduced with permission from ref. [60]. Copyright 2020, Wiley-VCH. (For interpretation of the references to color in this figure legend, the reader is referred to the web version of this article.)

subsequent sequence of reactions can occur. This implies that expanding the light-harvesting range of g-C_3N_4 increases the chances of producing more photogenerated carriers. Subsequently, we will elaborate on the different non-metal modification techniques performed to improve the photocatalytic activity and stability of g-C_3N_4.

3.1. Non-metal elements doped g-C_3N_4 composites

Doping is a conventional strategy used to adjust the electrical and optical characters of g-C_3N_4 at atomic level. Thereinto, non-metal doping is a common means to maintain the metal-free properties of g-C_3N_4, and can be divided into single-element doping and multi-element doping. Table 1 demonstrates the photocatalytic performance and stability of various non-metal element doped g-C_3N_4 composites. The introduction of non-metal elements with different electronegativity and atomic radius from C and N elements always changes the charge redistribution of g-C_3N_4, which may be one of the reasons for the improved catalytic performance. On the other hand, this may even cause a change in the bond length of the C—N bond as well. It is important to note that, however, the introduction of impurities may affect the stability of the g-C_3N_4 framework. Previous excellent results have confirmed that doping with non-metal elements can increase the delocalization of π-conjugated electrons and enhance visible-light utilization by decreasing its bandgap. Resulting increased dispersion of the contour distribution of LUMO and HOMO contributed to higher carrier mobility and charge separation [54]. These improvements enabled non-metal element doped g-C_3N_4 composites to have an enhanced photocatalytic performance.

3.1.1. Single-element doping

Previous articles showed that doping with transition metal atoms could effectively enhance the catalytic ability of g-C_3N_4, which was largely profit from the transition metal d-electron-induced local magnetism. However, some research findings demonstrated that boron-doped g-C_3N_4 (BCN) had semi-metal magnetism although it lacked d-electron, and BCN could also show extraordinary catalytic ability comparable to that of transition metal-doped g-C_3N_4 [55–57]. For such B-doped g-C_3N_4, the B atoms tended to be positioned in the center of the 3-s-triazine rings, rather than some metal atoms, such as aluminum and copper, which had a tendency to be situated above the center of 3-s-triazine rings [56]. Usually, B atoms were doped into large cavities by coordination with double-coordinated N atoms. In the same plane, the new electron transfer path from N to B was much easier

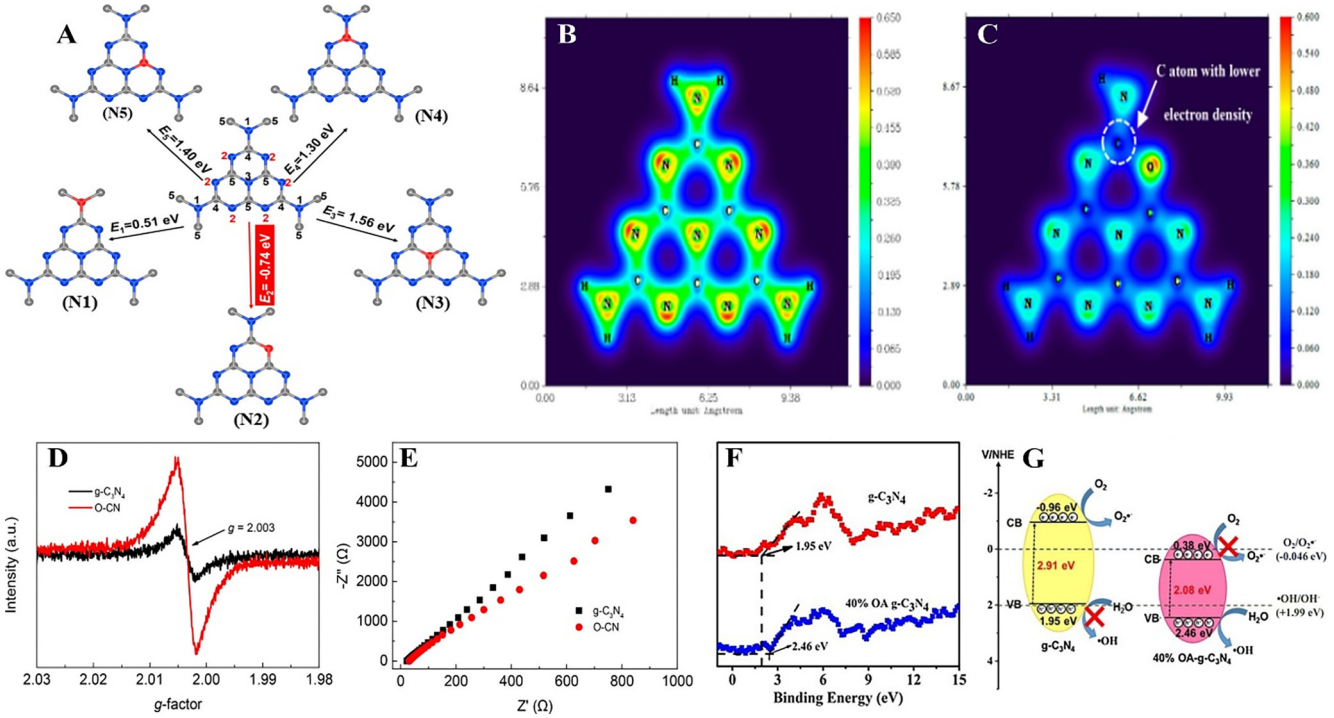

Fig. 3. (A) Calculated formation energy of OCN. Reproduced with permission from ref. [61]. Copyright 2015, Elsevier. (C, N and alternative O are represented by gray, blue and red spheres, respectively.) 2D valence-electron density color-filled maps of (B) g-C_3N_4 and (C) OCN. (C, N, O, and H are presented by gray, blue, red, and white spheres, respectively.) (D) Room-temperature EPR spectra and (E) EIS spectra of g-C_3N_4 and O–CN. Reproduced with permission from ref. [62]. Copyright 2018, American Chemical Society. (F) The valence band X-ray photoelectron spectroscopy and (G) the schematic band structure of g-C_3N_4 and 40 % OA-g-C_3N_4. Reproduced with permission from ref. [63]. Copyright 2017, Elsevier. (For interpretation of the references to color in this figure legend, the reader is referred to the web version of this article.)

than the path from N to C (Fig. 2A), which suggested that B doping could improve electronic excitation and localization [58]. The electronic and magnetic properties of BCN were studied using first-principles study and the results showed that B atoms could induce significant spin polarization on BCN, which was beneficial for O_2 activation (Fig. 2B-C) [59]. According to the ab initio molecular dynamics simulations, dissociating O_2 on BCN could occur by spontaneous under room temperature of 300 K. Additionally, the B atoms could be doped into g-C_3N_4 by replacing C atoms in the 3-s-triazine rings. B-doped g-C_3N_4 nanosheets could be manufactured by using dicyandiamide and B_2O_3 as reactants [60]. Available characterization results showed that instead of forming B − C bonds, the doped B atoms formed B–$(N)_3$ bonds and N_2 − BH bonds in BCN by substituting the corner- and bay-carbon sites (Fig. 2D-E). The constitution of B − N — C coordination in BCN due to doping of B atoms could firmly stabilize these exposed N atoms, which could be hydrogenated and promoted the synthesis of ammonia (NH_3).

In addition to the introduction of B atoms, the doping of O elements can also change the electronic structure of g-C_3N_4, resulting in an increased electron mobility. In a similar manner, the O atom also could be doped into g-C_3N_4 by displacing C or N atom. The five possible positions (marked as N1, N2, N3, N4 and N5) of the O atom in the O-doped g-C_3N_4 (OCN) and the corresponding formation energy were shown in Fig. 3A [61]. With an eye on the lowest formation energy, the substitution of N2 was much more advantageous than other conditions, which meant that the O atom preferred to displace the two-coordinated N atom. This was consistent with the findings of Lyu and co-workers [62]. Since the electronegativity of the O atom was higher than that of the N atom, the electronic structures of OCN changed when the O atom replaced the N atom, as evidenced in Fig. 3B-C. O atoms were more negatively charged, resulting in lower electron density for nearby C atoms. The EPR spectra (Fig. 3D) argued for a higher concentration of unpaired electrons in OCN. The EIS spectra of OCN and g-C_3N_4 in Fig. 3E displayed that the improved photocatalytic performance of OCN could be highly explained by the much smaller arc radius of OCN compared with g-C_3N_4, so OCN possessed more effective electrons transfer. Additionally, the introduction of heteroatoms had a remarkable impact on the energy band structure of semiconductors, which were strongly associated with the light utilization capability. Qiu et al. [63] manufactured O-doped porous g-C_3N_4 (OA-g-C_3N_4) via the condensation of urea and oxalic acid at high temperature. The experimental results showed that as a result of the doping of O atoms, the light adsorption edges of OA-g-C_3N_4 presented a significant red-shift. For another, the relative position between the energy band structure of the catalyst and the redox potential is closely related to the occurrence of the catalytic reaction. One of the disadvantages of pristine g-C_3N_4 is that the VB edge is slightly positive, giving it insufficient ability to split water under visible light irradiation. Tuning the energy band structure of the catalyst by the intervention of heteroatoms is one of the desirable methods. For example, the introduction of the O atoms shifted the VB edge of OA-g-C_3N_4 from 1.95 eV to 2.46 eV, as evidenced in Fig. 3F. This transition allowed the direct generation of·OH radicals during photocatalytic reactions, since the VB position of OA-g-C_3N_4 was more positive than the redox potential for·OH /OH^- (+1.99 eV vs NHE) (Fig. 3G). As for the·OH radicals, they were considerable and nonnegligible substances in the catalytic reactions. These predominant advantages had resulted in a significant enhancement in the photocatalytic activity of OA-g-C_3N_4.

For another, halogens (F, Cl, Br and I) were also frequently doped into g-C_3N_4 to modify its electronic structures. In detail, the doping of halogen atoms resulted in diverse density of states and repartition of the LUMO and HOMO. Yu et al. showed by DFT calculations that the system of doping halogen atoms into g-C_3N_4

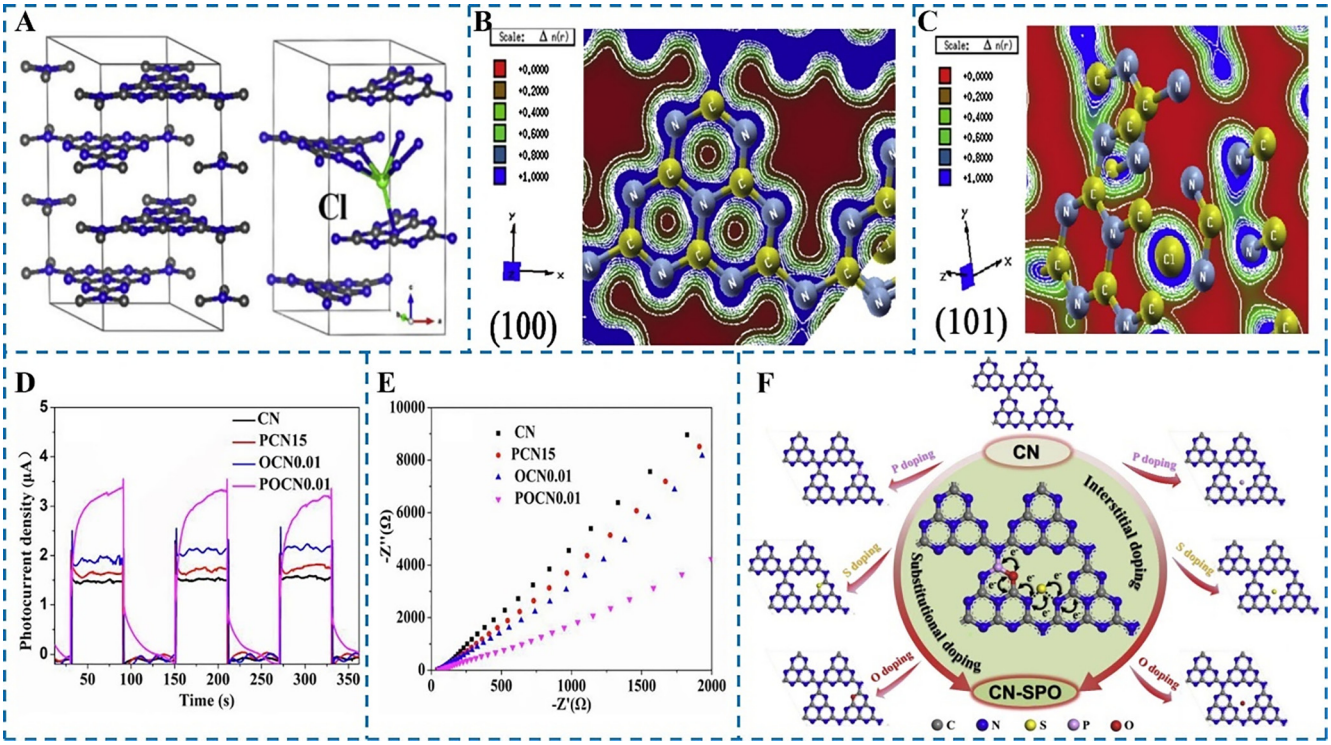

Fig. 4. (A) Crystal structure of pristine g-C_3N_4 and Cl-doped g-C_3N_4. Valence charge density in (B) (100) and (C) (101) crystallographic planes of Cl-C_3N_4. Reproduced with permission from ref. [65]. Copyright 2017, Elsevier. (D) Photocurrent responses and (E) electrochemical impedance spectra of CN, PCN15, OCN0.01 and POCN0.01. Reproduced with permission from ref. [69]. Copyright 2019, Elsevier. (F) The pathway for electron transport and proposed doping sites for the S, P and O atoms from DFT calculations. Reproduced with permission from ref. [75]. Copyright 2019, Elsevier.

by replacing C or N atoms in the 3-s-triazine rings was unstable. The most likely doping mode was interstitial doping with halogen atoms occupying the center of large cavities consisting of three 3-s-triazine rings [64]. The doping of halogen elements into the cavities minified the bandgap of g-C_3N_4. As the extremely high electronegativity of F atom, it tended to occupy the VB and HOMO, while the Cl, Br and I atoms tended to occupy the CB and LUMO. Also, with the increase of atomic number and the decrease of electronegativity, more electrons were moved from the halogen atoms to g-C_3N_4, which led to the decrease of work function, and that promoted the escape of electrons from g-C_3N_4 surface [64]. More interestingly, Liu et al. discovered that in addition to rest on the π-conjugate plane of g-C_3N_4, the Cl atom could be located at the interlayers and covalently bonded to g-C_3N_4 (Fig. 4A), acting as a bridge between the monolayer g-C_3N_4 sheets. As shown in Fig. 4-B-C, the intercalation of Cl atom changed the valence charge density and stretched the local 2D π-conjugated system of g-C_3N_4 to 3D space, which was beneficial for the charge carrier migration and separation process [65].

As mentioned above, heteroatoms doping could dramatically improve the catalytic performance of g-C_3N_4, but there were still many restrictions. Namely, the heteroatoms could act as defect sites for photoexcited e^-/h^+ recombination [66]. A possible approach to address this one drawback was self-doping for avoiding the introduction of any heteroatoms. Ran et al. [67] synthesized C self-doped g-C_3N_4 (CN-C) by the co-pyrolysis of urea and saccharose. The results of DFT calculations indicated the N atoms, used to attach to three 3-s-triazine rings, would be easily substituted by C atoms. The C self-doping with localized electrons could activate the response species, severely inhibit photoexcited e^-/h^+ pairs recombination and then improve the catalytic ability of g-C_3N_4. Meanwhile, several papers proved that this improvement could also be achieved by N self-doping, which could improve light absorption [68]. Self-doping can adjust the structural properties and electronic structures of g-C_3N_4 without introducing foreign heteroatoms, but the effects on its energy band structure and catalytic mechanism need to be investigated in depth.

In brief, we mainly discuss the effects of doping with non-metal elements including carbon, nitrogen, boron, oxygen, sulfur, phosphorus and halogens on the performance of g-C_3N_4 in this section, and substitutional and interstitial doping are the two main modes of these non-metal elements. In other words, one is replacing the C or N atoms of 3-s-triazine rings, the other is occupying the center of large cavities consisting of three 3-s-triazine rings. In contrast, halogens are more inclined to interstitial doping because of their larger atomic radius or electronegativity. Rational modulation of doping sites is essential for designing efficient catalysts. In the case of doped elements replacing the C atoms, the in-plane conjugation system of g-C_3N_4 may be weakened owing to the absence of graphitic carbon atoms, resulting in electron delocalization effect, thus, inhibiting the recombination of photogenerated carriers. Besides, since N and C have similar physicochemical properties, it is difficult for electrons to migrate from N to C. Doping of other elements can provide a new path for electron transfer, which may be an easier transfer path. As is known to all, the two major drawbacks of pristine g-C_3N_4 are the unsatisfactory visible light utilization and the rapid recombination of photogenerated carriers. Elemental doping, on the one hand, narrows the bandgap of g-C_3N_4 by elemental orbital doping thus extending its visible light utilization range. On the other hand, the recombination of photogenerated carriers is severely hindered by changing the electron transfer path. Thus, elemental doping is an efficient strategy to significantly improve the photocatalytic effect of g-C_3N_4. Notably, these non-metal elements can be doped into g-C_3N_4 at the same time to synergistically promote the photocatalytic effect, which will be discussed in detail in the next section.

3.1.2. Multi-element doping

Single non-metal element doping could overcome the inherent disadvantages and thus significantly enhanced the catalytic ability of bulk g-C_3N_4. Therefore, it was reasonable to speculate that multiple non-metal elements doping could recombine the points of single element doping to further improve the catalytic ability of g-C_3N_4. Surprisingly, this was indeed the case. To degrade fluoroquinolone antibiotics, Lv et al. fabricated a phosphorus and oxygen co-doped g-C_3N_4 (POCN) in a one-step thermal condensation manner [69]. The lone electron pairs of P atom replacing C atom delocalized to the P-doped 3-s-triazine ring, which promoted the Lewis acid sites creation. While the lone electron pairs of O atom replacing N atom delocalized to the O-doped aromatic system, which stimulated the charges mobility. All of these enabled POCN to enjoy a higher efficiency of charge separation (Fig. 4D-E) [69]. In 2018, Han et al. [70] prepared a sulfur and boron co-doped g-C_3N_4 via thermal treatment of the mixture of melamine, thiourea and boron oxide. Among the four samples, pure and doped g-C_3N_4, the co-doped g-C_3N_4 possessed the most sufficient separation yield of photoexcited e^-/h^+, which allowed it to show the highest removal activity for organic pollutants. The following year, they reported a phosphorus and boron co-doped g-C_3N_4 in a similar method. In the same way, the co-doped g-C_3N_4 degraded organic contaminants in wastewater such as dyes and antibiotics much better than pure and single element doped g-C_3N_4 [71]. Then, it has been documented that phosphorus and sulfur co-doped g-C_3N_4 significantly outperformed both pristine and corresponding single-element doped g-C_3N_4 in the field of photocatalytic H_2 production and degradation of organic contaminants [72–74].

Based on the demonstration that the catalytic ability of g-C_3N_4 could be substantially enhanced by doping with two non-metal elements, attempts have been made to dope with three non-metal elements simultaneously to further perfect its catalytic ability. In 2019, Liu et al. [75] successfully discovered (S, P, O) co-doped and exfoliated g-C_3N_4 nanosheets (CN-SPO). In this process, both substitutional doping and interstitial doping were involved. In more detail, in the 3-s-triazine rings, P atoms replaced the C atoms, O atoms displaced the N atoms, and S atoms took up the interstitial sites. Then, the photoexcited electrons could transfer through the P — O – C_1 – N_2 – S – N_2' (or N_2'–S – N_2 – C_1 – O — P) chain (Fig. 4F) between two abreast 3-s-triazine rings to expedite the separation of photoexcited carriers. Furthermore, ESR images showed that almost no TEMPO-e^- signal was detected for CN-SPO, and the TEMPO-h^+ intensity also was weaker, which once again indicated that CN-SPO had the highest photoexcited charge carrier reactivity.

Accordingly, doping with non-metal elements, which can adjust the electrical and optical attributes at atomic level to narrow the bandgap of g-C_3N_4, is one of facile and achievable methods to improve catalytic ability of g-C_3N_4. On the other hand, it must be

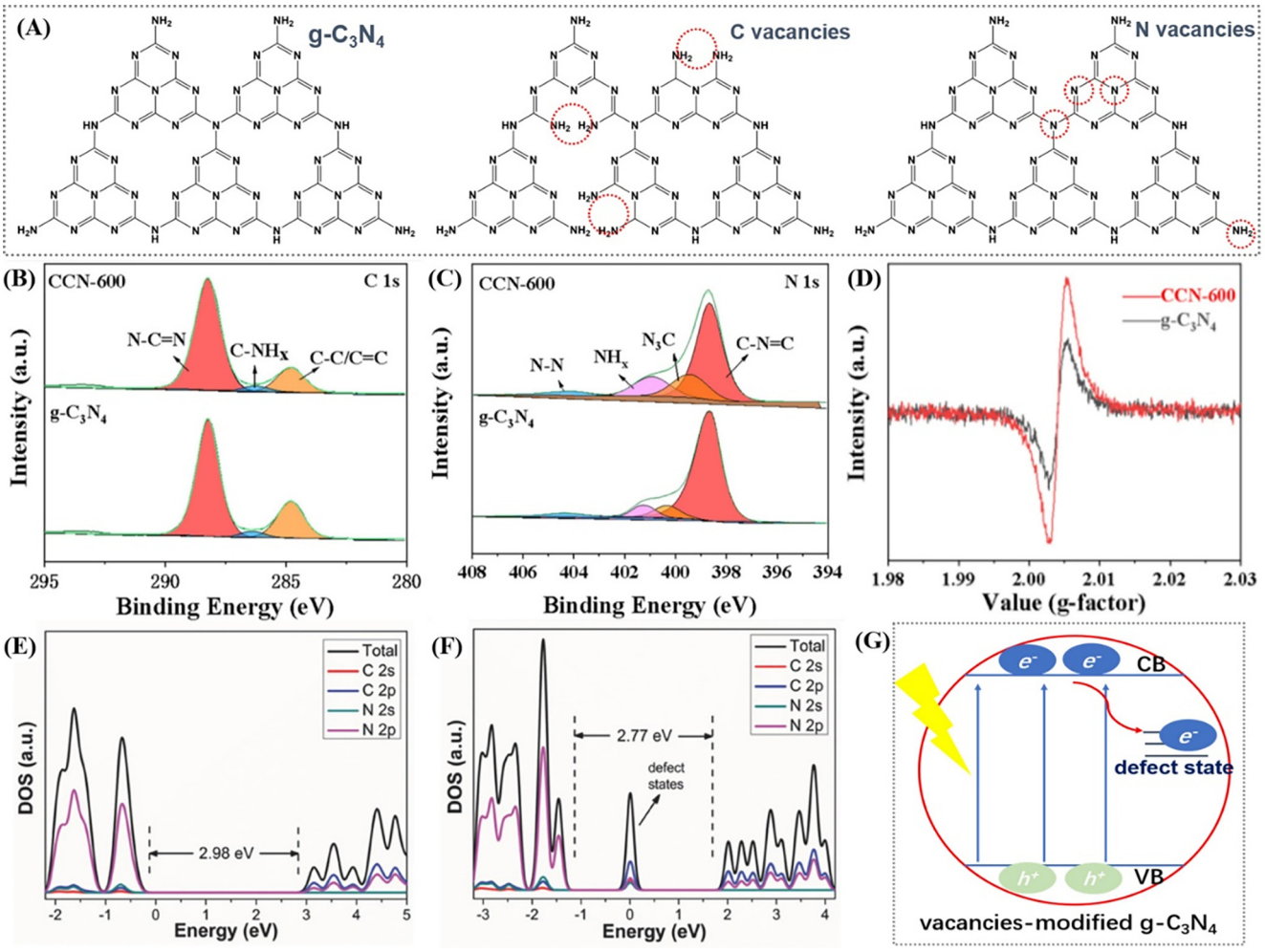

Fig. 5. (A) The possible positions where the vacancies occurred. High-resolution XPS spectra of (B) C 1 s and (C) N 1 s, and (D) ESR spectra of the pristine g-C_3N_4 and CCN-600. Reproduced with permission from ref. [97]. Copyright 2022, Elsevier. Density of states of (E) bulk g-C_3N_4 and (F) nitrogen defective g-C_3N_4. Reproduced with permission from ref. [100]. Copyright 2018, Wiley-VCH. (G) Schematic of the transfer of photogenerated electrons in vacancies-modified g-C_3N_4.

interesting to explore the effects of some unique doping of non-metal elements on the properties of g-C_3N_4, such as H [76], Si [77] and Se [78]. But, there is also a point that needs to be given great attention by researchers, which is that the introduction of heteroatoms can disrupt the original structure of g-C_3N_4, which may cause structural instability of the new material.

3.2. Vacancies modified g-C_3N_4 composites

Strikingly, theoretical and experimental results showed that vacancies introduction, which mainly including C vacancies and N vacancies, was also an effective strategy to narrow bandgap and facilitate photogenerated e^-/h^+ pairs separation [37,97]. Different from heteroatom doping, vacancies introduction did not introduce any impurities in the process of changing the frame structure of g-C_3N_4. Fig. 5A showed the possible positions of C vacancies and N vacancies. Normally, the absence of graphitic carbon atoms weakened the in-plane conjugation system of g-C_3N_4, and strongly modified the physicochemical properties of g-C_3N_4 by changing its frame structures. In other words, the absence of C atoms reduced the symmetry of g-C_3N_4, resulting in electron delocalization effects and defect states, which was favorable for the photogenerated electron transfer and promoting the carrier migration efficiency. More importantly, the introduction of C vacancies produced a large number of unsaturated N atoms, resulting in abundant -NH_x, which was beneficial for catalytic reactions. Tao et al. obtained C-vacancy modified g-C_3N_4 by calcining the samples at 600℃ (labeled as CCN-600) [97]. The high-resolution XPS spectra of C 1 s (Fig. 5B) and N 1 s (Fig. 5C) showed that the ratio of *N*-C═N bond to C—C/C═C bond and the content of amino (NH_x) were significantly increased, indicating the disappearance of some graphitic carbons. The EPR test (Fig. 5D) further confirmed the existence of carbon vacancies. Meanwhile, the peak intensity became stronger, suggesting that the recombination of photogenerated carriers can be markedly inhibited. Due to the introduction of C vacancies, the catalytic activity of photoreduction of O_2 to H_2O_2 can be increased by 14 times compared to pristine g-C_3N_4 [98].

By contrast, the introduction of N vacancies did not change the conjugate system of g-C_3N_4. As shown in Fig. 5A, four possible positions (C-N═C, N-$(C)_3$, bridging N and -NH_x) existed for the introduction of N vacancies, of which the N atoms in terminal -NH_x were the most likely to escape to form vacancies. In addition to this, the formation of vacancies in other positions caused the triple-coordinated carbon to convert to double-coordinated carbon. Furthermore, in comparison to N-$(C)_3$ and bridging N, the N atoms in C-N═C were more likely to escape to form nitrogen vacancies due to the lowest structural energy [99]. Shi and co-workers demonstrated by experimental result and theoretical calculation that the introduction of N vacancies introduced a defect state below the CB of g-C_3N_4 [100]. The defect state can accommodate the photoexcited electrons migrated from the VB of g-C_3N_4, which greatly inhibited the recombination of photogenerated carriers. The calculated density of states (DOS) of nitrogen defective g-C_3N_4 owned an evident decrease of intrinsic bandgap compared to bulk g-C_3N_4 (Fig. 5E-F), which facilitated the extension of the visible light reaction range of g-C_3N_4. On the other hand, the information of N vacancies can offer more active sites for O_2 adsorption to produce the $O_2^{\bullet-}$ [101,102], which can participate in a variety of catalytic reactions.

Briefly, vacancy engineering was an efficient measure to improve the photocatalytic performance by enhancing the inherent drawbacks of g-C_3N_4. Introducing vacancies in the tri-s-triazine rings of g-C_3N_4 can induce the narrowing of intrinsic bandgap and the formation of defect state, thus expanding the visible light response range and suppressing the recombination of photogenerated e^-/h^+ pairs (Fig. 5G). However, it was worth pointing out that the mechanism of induced vacancies generation was still unclear, which needed to be further explored in experimental studies.

3.3. Quantum dots modified g-C_3N_4 composites

Compared to modifications on the same material, coupling with other semiconductors is more likely to achieve suppression of photoexcited e^-/h^+ pairs recombination as the formation of junction interfaces. In which, one of the widely reported semiconductors is quantum dots (QDs). QDs are interesting 0D semiconductor materials that have recently received a lot of attentions from various disciplines due to their quantum size effects, dielectric confinement effects, and surface effects. By controlling the morphologies, structures and sizes of QDs, their energy gap can be readily tuned, which makes them potentially a promising co-photocatalyst [103–105]. Currently, there have many research results showed that QDs modified g-C_3N_4-based catalysts exhibited a better photoactivity than pristine g-C_3N_4. However, Cd(S, Se)/Zn(S, Se) QDs, which were extensively reported in the past, contained heavy metals and were harmful to the environment. In this section, we mainly discuss in detail the microstructures and properties of g-C_3N_4 modified by non-metal QDs, including carbon dots (CDs, mainly introduce carbon quantum dots (CQDs) and graphene quantum dots (GQDs)), black phosphorus quantum dots (BPQDs), boron nitride quantum dots (BNQDs) and g-C_3N_4 quantum dots (CNQDs). Table 2 demonstrates the enhanced properties of g-C_3N_4 modified by many non-metal QDs.

3.3.1. Carbon dots

CDs are luminescent carbon nanoparticles that are smaller than 10 nm in size at least one dimension, and are mainly composed of sp^2/sp^3 carbon. They have received increasing attention due to their up-conversion photoluminescence (UCPL), size tunability, and high water solubility [106]. Therefore, CDs have become increasingly popular co-photocatalysts, attracting a large number of researchers to explore the photocatalytic properties of CDs in combination with g-C_3N_4.

Loading CDs onto g-C_3N_4 could prominently improve the light utilization of CDs/g-C_3N_4 composites because of the UCPL and good photoinduced electron transfer properties of CDs. Mostly, 0D CDs loaded on g-C_3N_4 surface could convert light at wavelengths >550 nm to visible light <460 nm, thereby exciting g-C_3N_4 to produce more photoexcited e^-/h^+ pairs. In addition, the interaction of composites was the π-π stacking interaction, and this non-covalent interaction prevented the occurrence of defect at the junction interface of the two materials, resulting in a high-quality contact interface. Strikingly, the relative energy band alignment of CDs and g-C_3N_4 made it easy for photoexcited e^- to migrate from g-C_3N_4 to CDs, which suppressed the recombination of photoexcited carriers [107]. Meanwhile, the modification of CDs deformed the lattice of g-C_3N_4, and the introduced CDs could act as electron absorbers to inhibit photoexcited e^-/h^+ pairs recombination. However, when loaded with too many CDs, the CDs could again act as a recombination center to accelerate the recombination of photoexcited e^-/h^+, making the photocatalytic ability of the metal-free composite heavily reduced [108]. This was in accordance with the findings of Qu and his co-workers [109]. They reported that the bandgap of CDs/g-C_3N_4 composites would vary with the size and number of introduced CDs, in other words, the larger the lateral size of the CDs, the narrower the bandgap.

Actually, CQDs and GQDs, two typical types of CDs [110], were frequently used to modify g-C_3N_4 for improved its catalytic performance and stability. Hong et al. [111] loaded CQDs of average size of 5 nm onto g-C_3N_4 nanosheets surface. The prepared CQDs/g-C_3N_4 samples had a lower PL intensity, in other words, possessed

Table 2
The catalytic performances of some non-metal QDs modified g-C_3N_4 composites.

QDs	Catalyst	SSA (m^2/g) Improved / Pristine	Application	Efficiency Improved /Pristine	Reusability and stability (after 5 cycles)	Ref.
CDs	ag-C_3N_4-3 M/CDs	19.7 /14.6	photodegradation of Rh B	100 % /32 %	81 % after 4th	[126]
CDs	g-C_3N_4/CDs	–	photodegradation of phenol	100 % /50 %	no obvious deactivation	[107]
CDs	C-dots/g-C_3N_4	12 /10.3	photocatalytic Rh B degradation	3 times	no evident decrease	[108]
CQDs	C0.50 %/CN	48.495 /6.898	photodegradation of Rh B and TC-HCl	95.2 % /55.8 % 78.6 % /54.6 %	same activity	[111]
S-CQDs	HTCN-C(2)	32.982 /10.625	photocatalytic TC degradation	82.67 %/30.16 %	about 3.52 % lost	[127]
GQDs	s-g-C_3N_4@GQDs	–	electrocatalytic ORR	remarkably enhanced activity	activity declined after 8000 s	[128]
GQDs	GQDs/g-CNNR	–	photodegradation of OTC	80 % /47 %	no evident decrease	[129]
Hydroxyl-GQDs	GQDs/mpg-C_3N_4	71.3 /158.07	photodegradation of Rh B and TC	increase by 42 % (Rh B)	no apparent deactivation after 4th	[112]
NGQDs	NGQDs (1.66)/g-C_3N_4	–	photocatalytic H_2 evolution	139.6 /18.2 μmol h^{-1}	kept constant during 4 cycles	[130]
S, *N*-GQDs	g-C_3N_4/S, *N*-GQD	45.53 /52.99	photodegradation of Rh B	96 % /76 %	no obvious loss after 9th	[131]
g-C_3N_4 QDs	CNQDs/CN-20	–	photodegradation of Rh B	100 % /56 %	near 85 %	[125]
g-C_3N_4 QDs	g-C_3N_4/S-CNQDs	111.72 /27.58	photocatalytic MO degradation	100 % /30 %	no obvious change after 3rd	[132]
B doped g-C_3N_4 QDs	g-C_3N_4/BCNQDs	–	photocatalytic H_2 evolution	70.05 /1.2 μmol h^{-1}	no significant drop	[124]
B doped g-C_3N_4 QDs	g-C_3N_4/rGO/ BCNDs	52.13 /20.41	photocatalytic H_2 evolution	741.4 /12.2 μmol $g^{-1}h^{-1}$	slightly down	[133]
BPQDs	5 wt% BPQDs/g-C_3N_4	–	photocatalytic H_2 evolution	271 /48 μmol h^{-1} g^{-1}	no significant loss after 8th	[119]
BNQDs	BNQDs/UPCN	24.5 /6.2	photodegradation of OTC-HCl	82 % /31 %	77 % after 4th	[21]

a lower recombination rate of photoexcited e^-/h^+. Benefit by the UCPL properties of CQDs, the CQDs/g-C_3N_4 composites could generate more photoexcited e^-/h^+ when irradiated by light at wavelengths above 600 nm, making the photodegradation capacities several times higher than g-C_3N_4 [111]. The following year, another group at the same institution synthesized GQDs modified mesoporous g-C_3N_4 (GQDs/mpg-C_3N_4) and they also reached a similar conclusion [112]. By electrostatic attraction, the GQDs were uniformly dispersed on g-C_3N_4 planes, resulted in a gradual enhancement of visible light absorption of as-prepared GQDs/mpg-C_3N_4 composites from 450 nm to 800 nm.

The CDs modified g-C_3N_4 photocatalysts have displayed excellent performance, but in the process of application, researchers found that there are still some challenges, such as strict reaction conditions and low quantum yield of luminescence [113]. Then, it had been shown that heterogeneous doping with different non-metal elements (B [114], N [115], S [116] and P [117]) could lead to higher fluorescence intensity of CDs at different wavelengths. This had the potential to address the limitations of its low quantum yields. For instance, the *N*-doped GQDs absorbed visible and long wavelengths light much better than that of GQDs [46]. In addition, Seng et al. [118] synthesized *N*-doped CQDs (NCQDs) decorated 2D g-C_3N_4 by a simple hydrothermal route (Fig. 6A). The π-π interactions on the surfaces of NCQDs and g-C_3N_4 promoted their gradation efficiency under LED light irradiation.

3.3.2. Other quantum dots

The common non-metal QDs used to modify g-C_3N_4 were not only CDs but also some other quantum dots, such as BPQDs. BP, an allotrope of P, was a single-element 2D layered semiconductor material with many excellent properties, such as a direct-bandgap tunable with the number of layers (from 0.3 eV of bulk to 2.0 eV of monolayer), ultra-high mobility of photoexcited hole (as high as 1000 cm^2 V^{-1} s^{-1}) and relatively high SSA [119,120]. The direct-bandgap property of BP meant that it could be directly coupled with light, which drastically improved its light absorption efficiency and could be used directly as a photocatalyst [121]. The 0D BPQDs were formed as the lateral size of BP was reduced to less than 20 nm. Because of the quantum effects of BPQDs, they had more excellent properties than bulk BP, and many researchers had probed the co-catalytic properties of BPs and g-C_3N_4. On the first try, Kong et al. [122] introduced BPQDs to layered g-C_3N_4 surface by a high-vacuum stirring method. The corresponding charge distribution of the CB minimum (CBM) and VB maximum (VBM) in the real space (Fig. 6B) revealed that the CBM and VBM primarily came from g-C_3N_4 and BP, respectively. Under the action of the built-in electric field, the photoexcited electrons and holes would separately relocate to g-C_3N_4 and BP. That was, loading BP onto g-C_3N_4 surface could significantly stimulate photoexcited e^-/h^+ pairs separation, and severely suppress their recombination. However, a similar problem existed here. As shown in Fig. 6C-D, when the optimal loading content of BPQD was exceeded, the photocurrent response and photocatalytic efficiency of the composites were reduced due to the introduction of the recombination center of carriers.

BNQDs were another non-metal QDs ordinarily used to modify g-C_3N_4. Hexagonal boron nitride (h-BN) had a graphene-like structure and was known as "white graphene". The h-BN could be act as a promoter of photoexcited holes transferred to improve photocatalytic activities of h-BN/g-C_3N_4 composites. As the size of h-BN narrowed to quantum dot level, the quantum effect of BN quantum dots endowed them with intriguing fluorescence properties and dispersion. On the other hand, since the presence of many negative electron functional groups on BNQDs surface, such as some oxygen-containing groups, the BNQDs preferred to act as an attractor for photoexcited holes, thus, the BNQDs modified g-C_3N_4-based composites could synchronously accelerate both the separation of photoexcited e^-/h^+ pairs and the transfer of charges [21]. However, too much BNQDs could reduce photocatalytic efficiency (Fig. 6E) due to overlapping masking of reactive sites [123]. Surprisingly, g-C_3N_4 modified with CNQDs also exhibited more excellent photocatalytic properties. Just because the change of g-C_3N_4 morphology could also change its electronic band structure, so the separation and transfer of charges could be facilitated through the heterojunction interface between g-C_3N_4 and CNQDs [124]. Zhou and his colleagues [125] successfully produced g-C_3N_4 decorated by g-C_3N_4 quantum dots (CNQDs/CN) via a simple solvothermal technique. The as-prepared CNQDs/CN metal-free composites possessed an exceedingly high charge separation rate and long lifetime of pho-

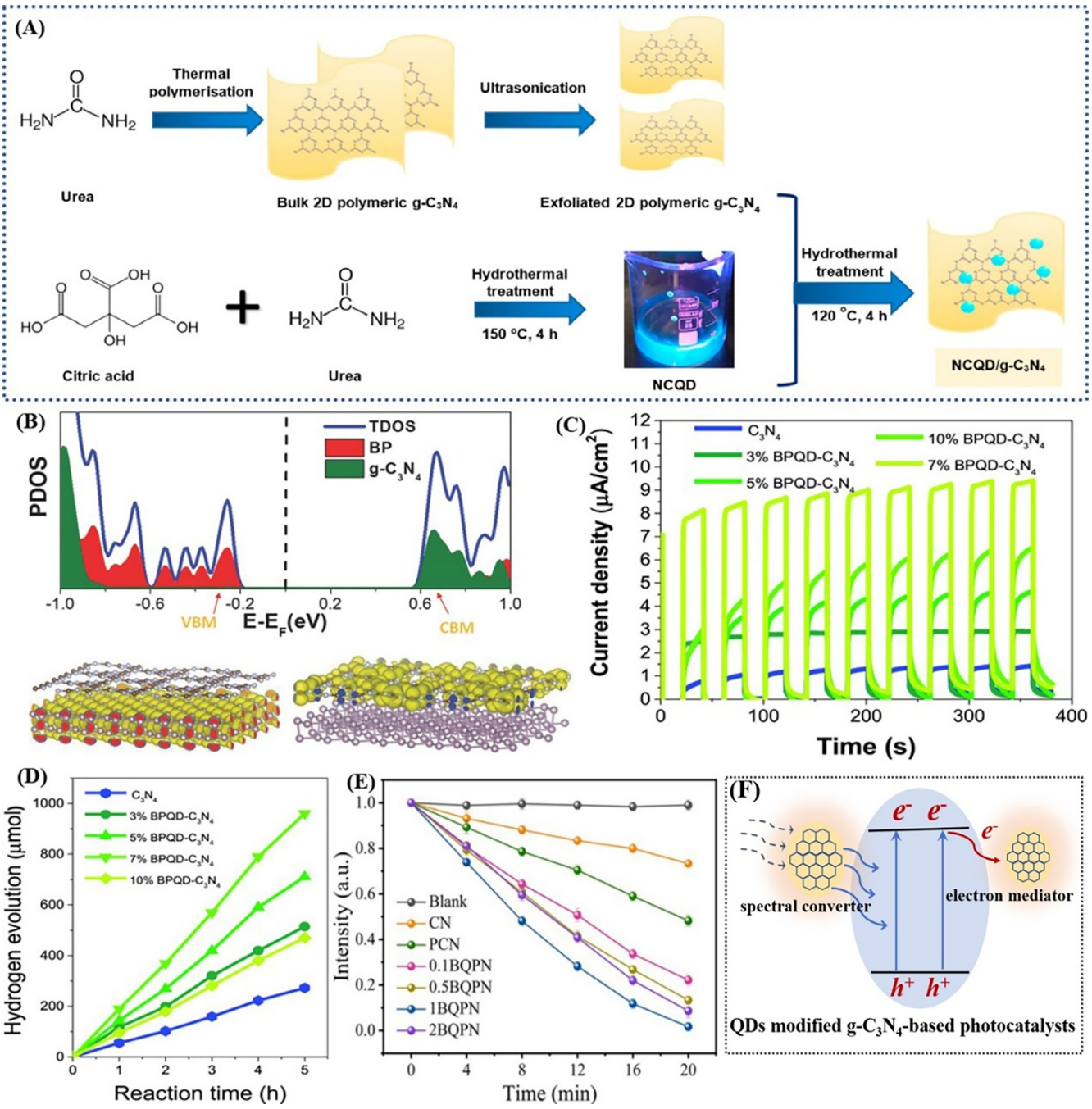

Fig. 6. (A) Schematic illustration of the hydrothermal route for NCQD/g-C_3N_4 composite synthesis. Reproduced with permission from ref. [118]. Copyright 2020, Elsevier. (B) DFT calculation studies of BP-C_3N_4 sample, the band structure and charge distribution of the VBM and CBM with an isovalue of 0.001 e $Å^{-3}$. (C) The photocurrent response of BPQD–C_3N_4 samples under study under the LED-420 irradiation with 0.2 V bias voltage conditions. (D) Photocatalytic H_2 generation of g-C_3N_4 and BPQD–C_3N_4 catalysts under simulated sunlight. Reproduced with permission from ref. [122]. Copyright 2018, Wiley-VCH. (E) Photocatalytic activity of the samples based on the photocatalytic degradation of naproxen. Reproduced with permission from ref. [123]. Copyright 2022, Elsevier. (F) The possible mechanism for enhanced photocatalysis of QDs modified g-C_3N_4-based photocatalysts.

toexcited charge carriers, which demonstrated favorable activity for photodegradation of rhodamine B. This self-modification strategy had proven to have many superior properties in the design of catalysts and could be greatly extended.

Thus, thanks to the modification of QDs, the performance of QDs modified g-C_3N_4-based photocatalysts has been improved to a great extent (Fig. 6F). In these catalysts, on the one hand, QDs can act as a spectral converter. When the photons energy is equal to or greater than the bandgap of g-C_3N_4, g-C_3N_4 can be excited to produce photogenerated e^-/h^+ pairs, and because g-C_3N_4 has a mild bandgap, only a portion of visible light can be used. The low efficiency of visible light utilization is a severe disadvantage that limits the catalytic performance of g-C_3N_4. QDs can absorb longer wavelengths of light, and then convert them into suitable wavelengths of light that can be used by g-C_3N_4, which can greatly improve the visible light utilization efficiency of g-C_3N_4. On the other hand, QDs can also be used as an electron mediator. In these composites, QDs, as another material distinct from g-C_3N_4, can work as a photoexcited electron absorber or holes attractor, in other words, as a carrier for photogenerated e^-/h^+ pairs separation

Table 3
The catalytic performances of some non-metal modified g-C_3N_4 composites.

Composite	Catalyst	SSA (m^2/g) Improved / Pristine	Application	Efficiency Improved /Pristine	Reusability and stability	Ref.
BP	8 %BP-g-C_3N_4	22.86 /28.44	photocatalytic removal of PPCPs	99.2 % /-	reduce to 95.9 % after 4th	[151]
BP	0.05BPCNS	51.8 /5.9	photocatalytic N_2 fixation	347.5 /23.7 μmol $L^{-1}h^{-1}$	no obvious decrease	[134]
PI	PI-g-C_3N_4	21.640 /9.287	photodegradation of BPA	96 % /6%	almost unchanged	[139]
PDI	CNPC3	28 /44.70	piezo-photocatalytic atrazine removal and H_2O_2 generation	94 % / 22.0 % 625.54 μM h^{-1} /-	decrease to 70 % after 4th -	[152]
rGO	g-C_3N_4/ rGO-N	158.5 /22.8	degradation of multiple pollutants	100 % /poor (AO7)	reduced after 4th	[140]
rGO	5 %rGO/g-C_3N_4	–	photocatalytic degradation of TC, β-naphthol and Rh B	3.89, 5.17 and 6.00 times	no obvious decrease (TC)	[153]
graphitic carbon	CN-20	92.6 /85.4	photocatalytic H_2 evolution	64 /15 μmol h^{-1}	no significant decrease after 4th	[141]
CNTs	SWCNTs/ CN	13.5 /5.3	photocatalytic H_2 production	3.4-fold	no obvious loss after 3rd	[142]
PEI	PEI/C_3N_4	–	photocatalytic water disinfection (*E. coli* and *E. faecalis*)	6.2 logs in 45 min /-4.2 logs in 60 min /-	slightly decrease after 3rd	[145]
PEI	PEI-g-C_3N_4 NSs	4.5 /-	detoxification of Cr(VI)	80 % /-	progressively decrease	[154]
lignin	LNRs/GCN-NRs	–	photodegradation of triclosan	99.20 % /-	decrease to 89.80 %	[155]
biphenyl diimide	g-C_3N_4/ BDI_{50}	–	photocatalytic H_2O_2 production	0.70 μmol h^{-1} /poor	–	[147]

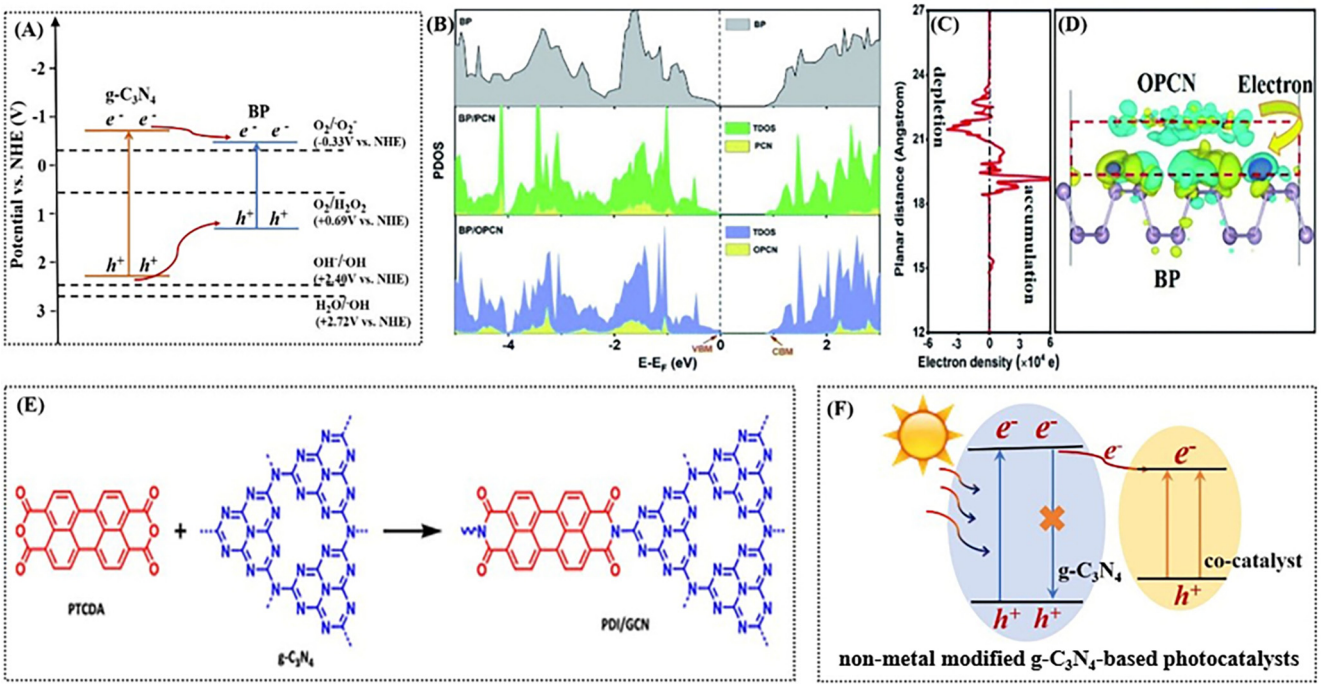

Fig. 7. (A) The schematic band structure of BP-g-C_3N_4. DFT calculation studies of the BP/OPCN heterojunction: (B) DOS, (C and D) differential charge density map and visualization of differential electron density at the BP/OPCN interface. The Fermi level is set to zero. Reproduced with permission from ref. [135]. Copyright 2020, Royal Society of Chemistry. (E) The synthetic route of PI-g-C_3N_4. Reproduced with permission from ref. [137]. Copyright 2018, American Chemical Society. (F) The possible photocatalytic mechanism on non-metal modified g-C_3N_4-based photocatalysts.

and suppress its recombination. Notably, it is worth pointing out that an excess of QDs again acts like a powerful magnet to promote the recombination of photogenerated carriers. Therefore, care must be taken to control the loading content of QDs during the material synthesis process. What is more, QDs with a similar π-conjugated structure to g-C_3N_4, such as CDs, can form exceptionally stable composites with g-C_3N_4 through strong interactions. These in turn have attracted more research interest for QDs modified g-C_3N_4-based catalysts. At the same time, the adverse effects of the QDs' own size and fluorescence effects on the catalytic efficiency have yet to be investigated in depth.

3.4. Other non-metal modified g-C_3N_4 composites

To maintain the metal-free properties of g-C_3N_4, exploring high-performance metal-free co-catalysts are an effort to perfect the photocatalytic efficiency of g-C_3N_4. Currently, numerous non-metals have been developed as co-catalysts. Table 3 exhibits the

catalytic performances of some non-metal modified g-C_3N_4 composites. As mentioned earlier, BP was an emerging promising 2D semiconductor material. In addition to the BP quantum dots, designing BP into other forms was also a desirable strategy, by way of example, the BP nanosheets. Qiu et al. [134] obtained BP nanosheets by liquid exfoliation of bulk BP, and as a co-catalyst, g-C_3N_4 nanosheets with BP nanosheets composites possessed an ultra-high catalytic activity. They deeply investigated the state of the binding bonds between the catalyst and co-catalyst. Results proved that the possible reason for improved photocatalytic activity was profit from the formation of C — P covalent bonds, which rearranged the electrons of composites and speeded up the electrons transfer. But in the other case, Hu and Ma et al. [135,136] reported that the formation of N — P bonds at the heterojunction interface was the possible key to improve the catalytic activity of composites. In fact, it was not surprising that different synthesis methods could affect the properties of the final products. In these BP/g-C_3N_4 composites, the CB edge of g-C_3N_4 was more negative than BP and the VB edge of g-C_3N_4 was more positive than BP (Fig. 7A). The photoinduced h^+ in g-C_3N_4 would transfer to BP, while the photoinduced e^- leaped from the VB to the CB of g-C_3N_4 and subsequently migrated to BP. Then, it is easy to generate $\cdot O_2^-$ radicals, since the CB potential of BP is negative enough. BP as a charge acceptor greatly inhibited carrier recombination. This was consistent with the findings of Hu and his colleagues. They studied the electron transfer direction at the BP/OPCN interface using the first-principles calculation (Fig. 7B-D). The photoinduced e^- in OPCN would rapidly migrate to the CB of BP [135].

Except for non-metal elements doping and non-metal quantum dots modification, up to now, researchers had developed many other non-metal materials to modify g-C_3N_4, and the more typical ones included coupling with perylene imide (PI). PI was a class of cheap and available *n*-type organic semiconductor, also known as perylene-3,4,9,10-tetracarboxylic imide. It could be usually synthesized by the reaction of its parent substance, perylene-3,4,9,10-tetracarboxylic dianhydride (PTCDA), with amine groups [137]. On account of the abundance of amine groups in g-C_3N_4, g-C_3N_4 modified by PI (PI-g-C_3N_4), an all-solid-state Z-scheme heterojunction, could be easily obtained by reacting the parent compound with g-C_3N_4 in N_2 atmosphere. Thanks to the π-conjugated electronic structures of both PDCTA and g-C_3N_4, they underwent surface hybridization by forming O═C − N − C═O covalent bonds, while g-C_3N_4 reacted with the unhybridized PDCTA through π-π stacking [137–139]. Fig. 7E showed the synthetic route of PI-g-C_3N_4. This was considerably different from g-C_3N_4 modified by BP nanosheets on different molecular layers. Dong et al. thus succeeded in getting PI-g-C_3N_4 for photocatalytic removal of NO. Owing to the modification of PI, the PI-g-C_3N_4 could utilize more visible light as emerging absorption bands around 500 and 550 nm, which made the PI-g-C_3N_4 possess better photocatalytic activity [138].

In fact, precisely because g-C_3N_4-based metal-free photocatalysts possess so many excellent properties that lots of modification methods have been tried to improve the photocatalytic abilities. Moreover, more and more non-metal materials have been developed as co-catalysts, for instance, graphene [140], graphitic carbon [141], carbon nanotubes [142], carbon nanospheres (CNS) [143], red phosphorus [144], polyethylenimine (PEI) [145], lignin [146], biphenyl diimide [147] and so on. Thereinto, CNS, usually prepared by hydrothermal treatment of carbon precursors within 160 ∼ 200 °C, have received considerable research interest [148]. Sun and his colleagues have demonstrated for the first time that CNS can be used as a promising co-catalyst to improve the photo-oxidation of g-C_3N_4 [149]. A stable connection can be formed between g-C_3N_4 and CNS, which facilitated the separation of photogenerated e^-/h^+ pairs. The modification of CNS can enhance the photocatalytic performance of the composites in several ways, including promoting the adsorption of substrates, enhancing the utilization of visible light, and facilitating the migration of electrons [150]. What is worth mentioning is that, however, new co-catalysts matched to the g-C_3N_4 energy level are of paramount importance. The presence of a co-catalyst can change the path of photogenerated electrons directly migrating from VB to CB of g-C_3N_4, thus alleviating the dilemma that photogenerated carriers are prone to recombination (Fig. 7F). Besides, a matched energy level is more conducive to the construction of a stable catalytic system. This may be an effort to develop a new co-catalyst.

Anyway, g-C_3N_4-based metal-free catalysts have been applied in various fields, and this will be detailed in the following section. Nevertheless, new approaches to modify g-C_3N_4 remain a hot research topic with the aim of further enhancing its catalytic performance and stability, which remains both an opportunity and a challenge from before to present and beyond.

4. Applications of g-C_3N_4-based metal-free catalysts

It is because g-C_3N_4-based non-metal photocatalysts exhibit these astounding properties that they have been widely applicated in many fields. In this chapter, we focus on the latest progress of g-C_3N_4-based non-metal photocatalysts for CO_2 reduction, NO_x purification, H_2O_2 production and bacterial disinfection, and especially the photocatalytic mechanisms are also described in detail.

4.1. CO_2 reduction

It is well known that CO_2 is one of the most common greenhouse gases, which can lead to evils such as global warming and ecological damage. If CO_2 could be converted into other useful gases in the presence of H_2O, such as carbon monoxide (CO), methane (CH_4) and formic acid (HCOOH), the emission of CO_2 would be controlled and resource utilization would be realized for the purposes of protecting environment and alleviating energy shortage [156–158]. To date, researchers have practiced many materials for CO_2 reduction, among which g-C_3N_4 notably stand out for its low cost, facile synthesis and environmental friendliness.

Photocatalytic CO_2 reduction utilizing solar energy was the most promising manner to simultaneously relieve the crises of worsening greenhouse effect and energy shortage. Thus, Fu et al. [159] fabricated O-doped g-C_3N_4 nanotube (OCN-Tube) for the photoreduction of CO_2 into hydrocarbon fuels (Fig. 8A). The O-doping endowed OCN-Tube a higher separation efficiency of photogenerated carriers. The results of DFT calculations showed that OCN-Tube had a narrowed bandgap as compared with bulk g-C_3N_4, indicating that OCN-Tube had wider visible-light absorption range. The optimized CB position of OCN-Tube (Fig. 8B) further satisfied the thermodynamic requirements of CO_2 reduction reaction. Besides, the adsorption energies of CO_2 on OCN-Tube and g-C_3N_4 were −0.21 and 0.02 eV, respectively. The more negative adsorption energy suggested that OCN-Tube possessed a stronger CO_2 adsorption capacity. As we all know, the CO_2 adsorption onto the photocatalyst surface was the first crucial process for CO_2 reduction reactions. As a result, owing to the O-doping, OCN-Tube exhibited an average CH_3OH productive rate of 0.88 μmol $g^{-1}h^{-1}$, which was about fivefold higher than that of g-C_3N_4 (0.17 μmol $g^{-1}h^{-1}$). Fu et al. [58] declared that the CO_2 adsorption free energy on the B sites of BCN was − 2.2 eV. Both $^{12}CH_4$ and ^{12}CO were detected when $^{12}CO_2$ gas was used as the reactant, and the CH_4 yield of 1 % BCN was roughly 32 times better than g-C_3N_4. Particularly, a p-type BCN_x could be used for photoelectrochemical CO_2 reduction [160], and various kinds of products could be detected as the CB potential of $BCN_{1.5}$ was high enough. However, from the experi-

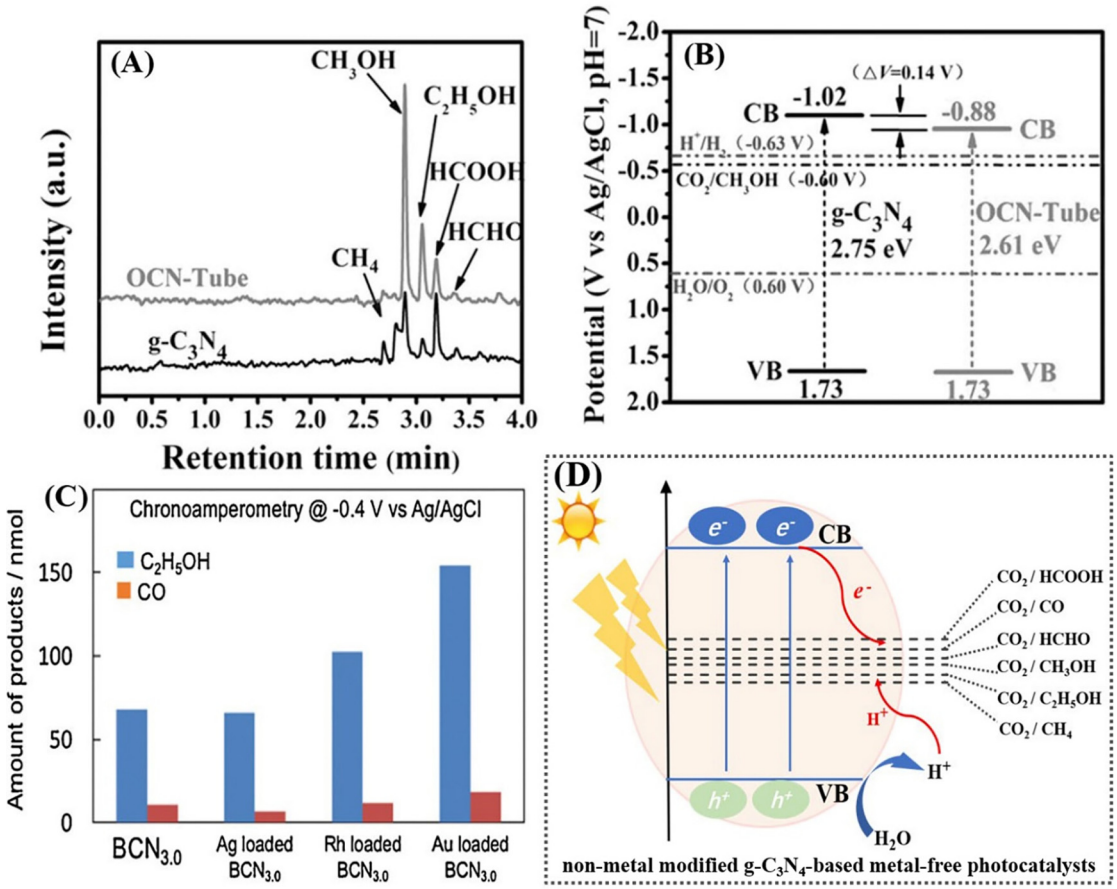

Fig. 8. (A) Original chromatograms of the gas products from bulk g-C_3N_4 and OCN-Tube after 1 h irradiation. (B) Band alignments of bulk g-C_3N_4 and OCN-Tube versus the saturated Ag/AgCl reference electrode. Reproduced with permission from ref. [159]. Copyright 2017, Wiley-VCH. (C) Products analyses of photoelectrochemical reduction of CO_2 over co-catalyst loaded $BCN_{3.0}$ electrodes. Reproduced with permission from ref. [160]. Copyright 2016, Elsevier. (D) Schematic diagram of photocatalytic CO_2 reduction based on g-C_3N_4-based metal-free photocatalysts.

mental results of the comparison experiments with loaded metal co-catalysts (Fig. 8C), we found a disadvantage of g-C_3N_4-based metal-free catalysts that the catalytic performance was far inferior to that of the metal-containing catalysts. Once again, we were reminded that improving the catalytic performance of non-metal g-C_3N_4-based catalysts was the critical key to expanding their practical applications.

As shown in Fig. 8D, photocatalytic CO_2 reduction was a complicated process involving multiple electrons. Non-metal modifications can extend the visible light utilization of g-C_3N_4. In addition, the bandgap of the modified g-C_3N_4 allowed it to meet the thermodynamic requirements of various reactions. In detail, under visible light or UV irradiation, the g-C_3N_4-based photocatalysts were motivated and generated e^-/h^+, and then, CO_2 adsorbed on the surface of g-C_3N_4-based materials could be reduced to other substances. Even reacted continuously along the reaction path of $CO_2 \rightarrow HCOOH \rightarrow HCHO \rightarrow CH_3OH \rightarrow CH_4$ in the presence of photoexcited e^- [161]. Generally, the process of g-C_3N_4-based non-metal materials (CN-X) for CO_2 photoreduction mainly involved the following eight equations:

$$CN\text{-}X + h\upsilon \rightarrow e^- + h^+ \quad (1)$$

$$H_2O + 2\,h^+ \rightarrow 1/2O_2 + 2H^+ \quad (2)$$

$$CO_2 + 2H^+ + 2e^- \rightarrow CO + H_2O \quad (3)$$

$$CO_2 + 8H^+ + 8e^- \rightarrow CH_4 + 2H_2O \quad (4)$$

$$CO_2 + 2H^+ + 2e^- \rightarrow HCOOH \quad (5)$$

$$CO_2 + 4H^+ + 4e^- \rightarrow HCHO + H_2O \quad (6)$$

$$CO_2 + 6H^+ + 6e^- \rightarrow CH_3OH + H_2O \quad (7)$$

$$2CO_2 + 12H^+ + 12e^- \rightarrow C_2H_5OH + 3H_2O \quad (8)$$

The improvement of electron utilization and carrier separation efficiency was crucial for photocatalytic CO_2 reduction of g-C_3N_4-based materials. BPQDs-modified g-C_3N_4 composites assembled by electrostatic attraction demonstrated superb performance in photocatalytic CO_2 reduction for CO production [162]. In a further development, the OCN modified by CQDs possessed a remarkable ability of photocatalytic CO_2 reduction to CH_4 [163]. The introduction of CQDs increased the CO_2 adsorption site, and the oxygen doping promoted the dissociation of H_2O to produce more sustainable supply of H^+. Thus, these enabled the best selected sample to have a CH_4 productivity 14-fold higher than pure g-C_3N_4. Furthermore, 3D macropore C-vacancy g-C_3N_4 was synthesized by using polymethylmethacrylate as a template for CO_2 photoreduction [164]. The macropore structure increased the SSA and therefore offered extensive catalytic active sites. The introduction of carbon-vacancy restrained the recombination of photoexcited e^-/h^+ pairs and therefore raised the utilization of surface carriers.

In summary, positive control of total CO_2 in the atmosphere to alleviate the energy crisis remains an urgent research topic for us. The photocatalytic conversion of CO_2 to clean hydrocarbon fuels

using g-C_3N_4-based metal-free catalysts is one of the most desirable methods, but there is still a long way to go from the laboratory to factory, which requires our sustaining and unremitting efforts.

4.2. NO_x purification

Excessive NO_x emission is extremely damaging to the environment, as it is one of the main substances in the formation of acid rain and photochemical smog, as well as an important factor in the destruction of the ozone layer. As is known to all, nitrogen monoxide (NO) could not be directly oxidized without catalysts. But it has been proven in literatures that when exposed to visible light, it could be photo-oxidized into NO_2^- or NO_3^- when a photocatalyst is present [67]. Meanwhile, g-C_3N_4 as a cheap photocatalyst has gained much attention on NO_x purification in recent years. Li et al. [165] used DFT theoretical calculations and experimental facts to demonstrate that g-C_3N_4 could efficiently remove NO in the presence of light.

Researchers also explored the removal of NO_x by non-metal modified g-C_3N_4. For example, S-doped and carbon-vacancies co-modified g-C_3N_4 was lightly synthesized for NO_x removal using desulfurization waste liquid [166]. Fig. 9A showed the photocatalytic mechanisms of NO_x purification. The adsorption of NO and O_2 was a key to the ability of photocatalysts to remove NO_x. This non-metal modification strategy resulted in an increased electrons density on the material surface and improved the separation as well as transfer efficiency of photocarriers, then suppressed production of intermediate toxic products, nitrogen dioxide (NO_2). Thus it enhanced the adsorption of NO and activation of O_2, which could contribute to generate more reactive oxygen species (ROS), for example,·OH,$\cdot O_2^-$ and so on. Finally, NO_x could be oxidized by these ROS, and converted into NO_2^- and NO_3^-. Typically, the process of CN-X for NO removal mainly involved the following equations:

$$\text{CN-X} + h\upsilon \rightarrow e^- + h^+ \quad (9)$$

$$O_2 + e^- \rightarrow \cdot O_2^- \quad (10)$$

$$\cdot O_2^- + 2H^+ + e^- \rightarrow H_2O_2 \quad (11)$$

$$H_2O_2 + e^- \rightarrow \cdot OH + OH^- \quad (12)$$

$$NO + 1/2 \cdot O_2^- \rightarrow NO_2 \quad (13)$$

$$NO + \cdot OH \rightarrow HNO_2 \quad (14)$$

$$NO_2 + \cdot OH \rightarrow HNO_3 \quad (15)$$

From the foregoing, in the process of photocatalytic NO_x purification, the main ROS were $\cdot O_2^-$ and ·OH and the main final products were NO_2 and HNO_3. However, NO_2 was more toxic than NO. Fortunately, recent experimental results have shown that non-metal modified g-C_3N_4-based composites could also catalyze the conversion of NO to nitrogen (N_2). Dong et al. synthesized C vacancy-modified g-C_3N_4 nanosheet (Ns-g-C_3N_4) for efficient and selective photoreduction NO to N_2 [167]. The NO concentration variation followed first-order kinetics, and the removal rate over Ns-g-C_3N_4 was 5-fold higher than that of g-C_3N_4 (Fig. 9B-C). DFT simulations proved that the C vacancies on the Ns-g-C_3N_4 can be used on the one hand as traps for photoexcited e^-, and on the other hand as chemical adsorption sites for NO. The photocatalytic mechanism can be described as follows (Fig. 9D): (i) NO was adsorbed onto the surface of Ns-g-C_3N_4 by C_v—O—N interactions. (ii) The O—N single bond of Cv—O—N was broken by photoexcited e^-, thus releasing decomposed N and O, which further formed N_2 and O_2. It was thanks to the non-metal modification that Ns-g-C_3N_4 exhibited efficient and selective photoreduction of NO to N_2, whereas pristine g-C_3N_4 can only lead to photoxidation of NO to NO_2. Furthermore, photocatalytic N_2 fixation to produce NH_3 was extremely desirable [168]. Wang et al. successfully fabricated BCN for photocatalytic N_2 reduction to NH_3 synthesis and improved the yield of NH_3 by a factor of 10 [60]. To sum up, it was an effective strategy to use non-metal modified g-C_3N_4 for photocatalytic NO_x purification and N_2 fixation, and it was considered to pave a new research way for air pollution. At the same time, from the results of the cyclic experiments, we can see that although these modifications improve the catalytic performance of g-C_3N_4, the stability of these materials need to be enhanced, which may find a way out from the combination with theoretical calculations.

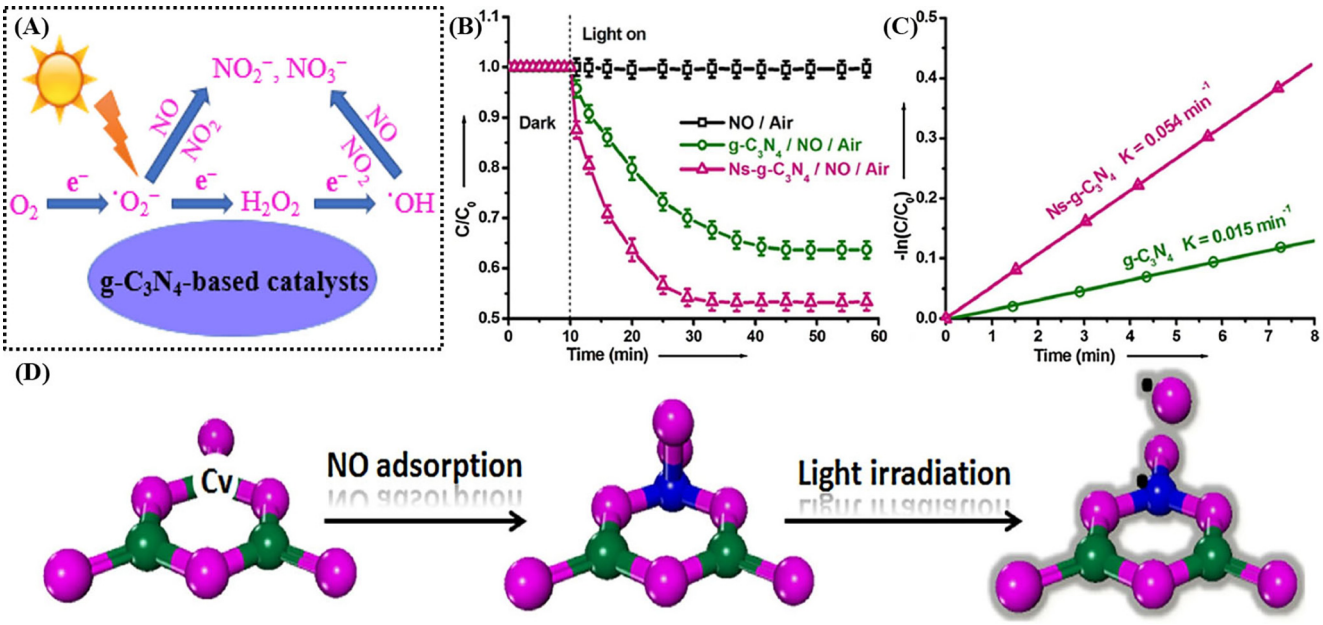

Fig. 9. (A) Possible mechanisms for photocatalytic NO_x removal by g-C_3N_4-based non-metal materials. (B) The relative change of NO concentration (C/C_0) as a function of irradiation time tested over g-C_3N_4 and Ns-g-C_3N_4. (C)First order kinetics fitting for the data obtained from g-C_3N_4 and Ns-g-C3N4. (D) The decomposition process of NO on the surface of Ns-g-C_3N_4. Reproduced with permission from ref. [167]. Copyright 2017, Elsevier.

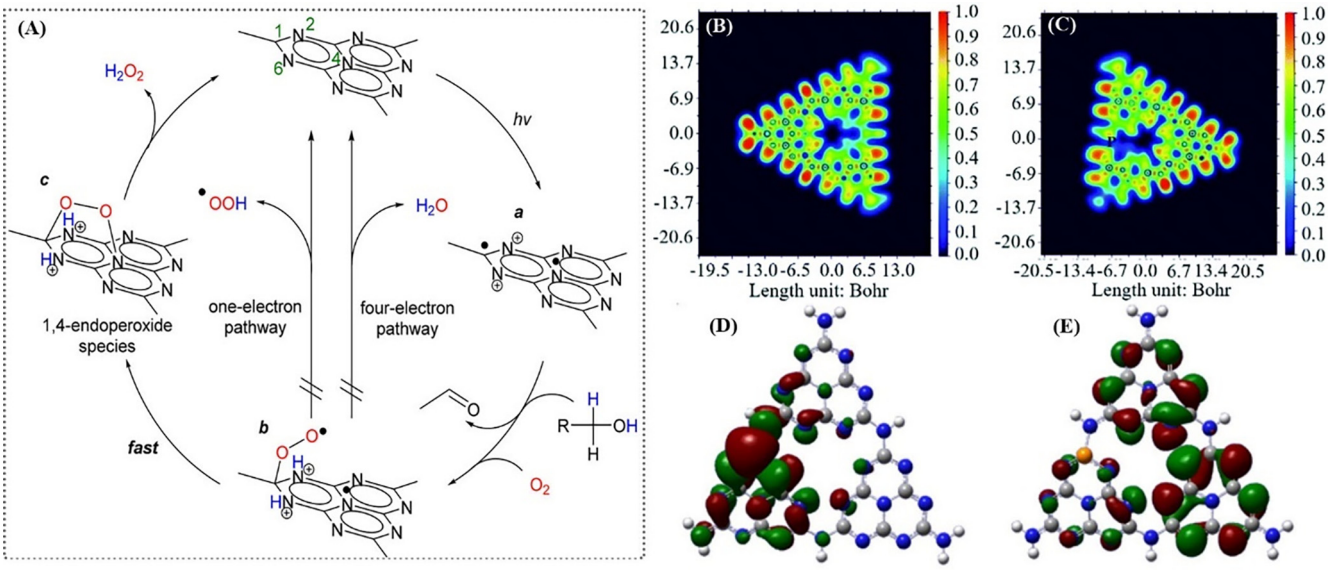

Fig. 10. (A) Proposed mechanism for selective formation of H_2O_2 on the photoactivated g-C_3N_4 surface. Reproduced with permission from ref. [172]. Copyright 2015, American Chemical Society. Color filled map of the electron localization function of (B) g-C_3N_4 and (C) PCNHS. (D) LUMO) and (E) HOMO of PCNHS. The isosurface is taken at a value of 0.002 e/Bohr3. Reproduced with permission from ref. [173]. Copyright 2020, Royal Society of Chemistry.

4.3. H_2O_2 production

H_2O_2, with H_2O and O_2 as by-products, has received much interest as a promising clean energy alternative. Traditional synthesis methods of H_2O_2 based on anthraquinone method or noble metal catalytic systems consume a great deal of energy or are likely to engage in hazardous H_2/O_2 mixed substances. Thus, it is inevitable to develop economical and green synthesis methods. The direct conversion of light-driven H_2O and O_2 to H_2O_2 is a process that occurs slowly or difficulty, but the use of catalysts can accelerate this process. Stunningly, numerous existing research results indicated that g-C_3N_4 was an ideal photocatalyst for photocatalytic reduction of O_2 for H_2O_2 production [169–171].

Usually, the photocatalytic O_2 reduction to H_2O_2 generation process required the use of sacrificial agents as proton donors, and the most commonly used sacrificial agents were alcohols. Meanwhile, as shown in Fig. 10A, there was the process of single-electron reduction of O_2 to·OOH generation, which inhibited the production of H_2O_2. Therefore, efficient and rapid synthesis of 1,4-endoperoxide species by double-electron reduction of O_2 was the key to perfect the efficiency of H_2O_2 selectivity [172]. For instance, a P-doped g-C_3N_4 hollow spheres (PCNHS) was applied to the selective synthesis of H_2O_2 [173]. The results of electron localization function (Fig. 10B-C) showed that compared to pristine g-C_3N_4, electrons were more easily delocalized to other zones in PCNHS. Furthermore, the LUMO and HOMO delocalization (Fig. 10-D-E) has been reinforced by P-doping. These adjustments have allowed the PCNHS to demonstrate an improved carrier mobility and a suppressed recombination rate of carriers. In this case, the results certified the doped P substantially promoted 1,4-endoperoxide species formation, resulting in the H_2O_2 yields of 1684 μmol $g^{-1}h^{-1}$ with isopropanol as proton donor, which was 11.2 times more than g-C_3N_4. Then Wei and his co-workers [174] probed that oxygen-enriched g-C_3N_4 also displayed excellent photocatalytic H_2O_2 production performance and EPR spectra demonstrated that 1,4-endoperoxide species rather than·OOH were produced in this process. This again confirmed the above discussion.

It was interesting to note that some research results have proved that photocatalytic H_2O_2 generation could also proceed through a consecutive two-step single-electron O_2 reduction reaction ($O_2 + e^- \rightarrow {\cdot}O_2^-$,${\cdot}O_2^- + 2H^+ + e^- \rightarrow H_2O_2$) [175]. Zhao et al. [176] reported that combining g-C_3N_4 with carbon nanotubes (CNTs) by amidation reaction could tune the CB level of g-C_3N_4. Specifically, there was a negative shift of CB level when formed g-C_3N_4/CNTs, which could make a sufficient potential difference from single-electron reduction of O_2 to·O_2^-, thereby promoting the ability of H_2O_2 generation. In addition, considering that the use of sacrificial agents would increase the cost, the researchers were again working on the synthesis of H_2O_2 without any sacrificial agents. A common substitution method currently used was the catalytic conversion of H_2O and O_2 to H_2O_2, which has 100 % atomic efficiency. In this catalytic system, firstly, H_2O was oxidized to the generation of H^+ and O_2, and then, H_2O_2 was produced by a double-electron O_2 reduction reaction ($2H_2O + 4\ h^+ \rightarrow 4H^+ + O_2$, $O_2 + 2H^+ + 2e^- \rightarrow H_2O_2$) [169,177]. However, it was easy to find that in terms of the efficiency of H_2O_2 production, it was much better with the sacrificial agents than without them. In brief, although a lot of efforts have been done on H_2O_2 generation, there are still many challenges to be solved. Typically, much experimental and theoretical work needs to devoted to further reveal the reaction mechanism, which will facilitate our precise preparation for further promoting the efficiency of H_2O_2 production.

4.4. Bacterial disinfection

Infectious diseases caused by pathogenic bacteria such as viruses, bacteria and fungus in the water environment pose a serious threat to human health. Meanwhile, it is urgent to develop effective and economical water/wastewater disinfection technologies to alleviate the shortage of water resources worldwide. The photocatalytic water disinfection based on non-metal semiconductor photocatalysts has an incomparable excellent bacterial inactivation effect than traditional disinfection methods, and they have the advantage of killing most pathogenic bacteria without producing toxic by-products [178,179]. Among them, g-C_3N_4 has been applied in the exploration of photocatalytic water disinfection. For example, Ding et al. [180] used g-C_3N_4 to inactivate multiple antibiotic-resistant bacteria isolated and purified from secondary wastewater, and gained promising outcomes.

Experimental and theoretical results suggested that the bactericidal activities of g-C_3N_4-based photocatalysts were mainly achieved via generating ROS with strong oxidization (Fig. 11A), such as $^{\cdot}OH$, $^{\cdot}O_2^-$ and H_2O_2, that bound directly or indirectly to bacterial cells [181]. The destruction of cell membranes and walls suggested the important role of the ROS in the photocatalytic disinfection. Currently, two strategies were commonly used to perfect the photocatalytic water disinfection ability of g-C_3N_4. The first was to tune the position of CB of g-C_3N_4 to produce more and longer lifetime ROS. The second was to strengthen the interaction between bacteria and g-C_3N_4-based materials. Based on the above considerations, Teng et al. [182] declare that edge-functionalized

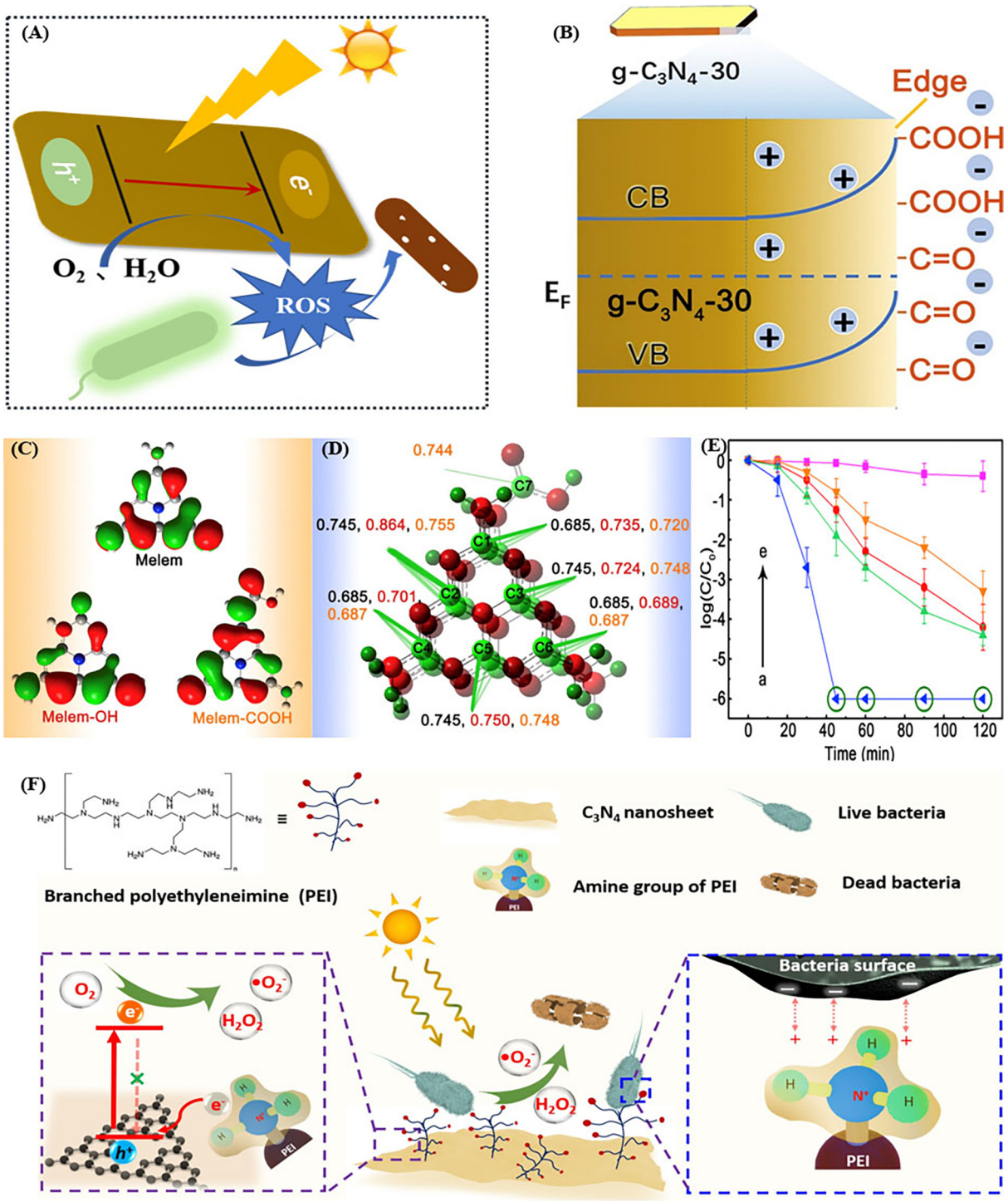

Fig. 11. (A) The possible mechanism of photocatalytic disinfection on g-C_3N_4-based metal-free photocatalysts. (B) Schematic diag ram of possible depletion layer and the band-bending effects near the edge of g-C_3N_4-30. (C) HOMO of M^+_{elem}, M_{elem}-OH^+, and M_{elem}-$COOH^+$. (D) Mulliken charge distribution of different C atoms in M^+_{elem} (black numbers), M_{elem}-OH^+ (red numbers), and M_{elem}-$COOH^+$ (orange numbers). (E) The disinfection performances of films of different g-C_3N_4 samples with different oxidization degrees under full-spectrum solar-light irradiation. (a, g-C_3N_4-30; b, g-C_3N_4-reduction; c, g-C_3N_4-45; d, g-C_3N_4-60; e, bulk-g-C_3N_4) Reproduced with permission with permission from ref. [182]. Copyright 2019, Elsevier. (F) Illustration of the roles of PEI on C_3N_4 for enhanced photocatalytic bactericidal activity. Reproduced with permission from ref. [145]. Copyright 2020, Elsevier. (For interpretation of the references to color in this figure legend, the reader is referred to the web version of this article.)

g-C_3N_4 nanosheets exhibited excellent bacterial inactivation performance. On the one hand, ESR spectrum showed as-prepared photocatalysts possessed a stronger signal of $\cdot O_2^-$, because the introduction of electron withdrawing groups at the margins of g-C_3N_4 nanosheets, which bended their energy band upward (Fig. 11B), and thus enhanced the generation of H_2O_2. On the other hand, the edge functionalization induced an anisotropic built-in electric field, which inhibited photoexcited e^-/h^+ pairs recombination. DFT calculations further certified that the functional groups can enhance the charge separation efficiency by changing the orbital status of neighboring C atoms (Fig. 11C-D), resulting that the photogenerated e^- favored to gather at the edge of g-C_3N_4 nanosheets. In aqueous solution, H_2O_2 had a remarkably long lifetime, so this g-C_3N_4 nanosheets exhibited admirable disinfection performance (Fig. 11E) with a first-order disinfection rate of 0.081 min^{-1} (R^2 = 0.90). And Zeng et al. [145] enhanced the photocatalytic bactericidal ability of g-C_3N_4 through PEI modification. The presence of amino groups on PEI promoted the production of long lifespan ROS ($\cdot O_2^-$ and H_2O_2), as well as enhanced the interaction between bacteria and photocatalysts through electrostatic adhesion (Fig. 11F). These two aspects made the PEI/g-C_3N_4 composites had efficient inactivation for both gram-negative *Escherichia coli* and gram-positive *Enterococcus faecalis*.

H_2O_2 was a crucial disinfectant for achieving efficient bacterial inactivation, and it was clear from the above description that H_2O_2 could be produced by both a consecutive two-step single-electron and one-step double-electron O_2 reduction reaction. Further, Xiao and co-workers reported that by introducing a large amount of surface amino groups to synthesize amino-rich holey ultrathin g-C_3N_4 nanosheets (AHUCN) [183], this could lead to a transformation of O_2 reduction path from two-step single-electron reduction to one-step double-electron reduction. This transformation greatly improved the disinfection efficiency due to the stimulated generation of H_2O_2. The results showed that AHUCN was able to completely inactivate *Escherichia coli* within 2 h, where H_2O_2 was the dominant species. And it was in possession of the strongest inactivation rate compared to previously studied g-C_3N_4-based photocatalysts.

In addition to these strains, g-C_3N_4-based metal-free photocatalysts had good bactericidal activity against many species of bacteria. For example, Tang and co-workers fabricated CQDs/g-C_3N_4 heterojunctions for *Staphylococcus aureus* inactivation in vitro and in vivo [184]. More importantly, toxicity analyses confirmed it had excellent non-toxicity. Then, a O-doped g-C_3N_4/hydrothermal carbonation carbon heterojunction photocatalyst was employed for human adenovirus type 2 inactivation, where·OH was the dominated ROS [185]. Besides, as we all know, both chemical oxidation and physical action were known to produce damage to microorganisms. Unsatisfactorily, most of the current literatures were devoted to expose the photocatalytic performance of g-C_3N_4 for disinfection, while few studies had investigated the physical action of g-C_3N_4-based materials for disinfection, such as prepared sharp edges. One promising approach was physical damage first led to bacterial cell membrane rupture and cell death, and then radicals oxidized various components of the cell. Presumably this synergistic effect of physical damage and ROS oxidation could achieve rapid inactivation of pathogenic bacteria in water, and this was bound to be really interesting.

In conclusion, g-C_3N_4-based metal-free photocatalysts have demonstrated excellent application prospects in CO_2 reduction, NO_x purification, H_2O_2 production and bacterial disinfection. The CB position of the photocatalyst satisfying the thermodynamic requirements for the selective reduction of CO_2 is a prerequisite for photocatalytic reducing of CO_2 to useful substances. Simultaneously, the amount of CO_2 adsorption by the photocatalyst is one of the important factors affecting the efficiency of photocatalytic CO_2 reduction. Likewise, the adsorption capacity of NO and the activation capacity of O_2 can directly affect the catalytic efficiency of photocatalytic NO reduction. Generally speaking, the larger the SSA of the catalyst, the greater the adsorption capacity of the gas. Therefore, increasing the SSA of g-C_3N_4-based metal-free photocatalysts is one of the feasible strategies to enhance its photocatalytic efficiency. In addition, H_2O_2 can be generated by one-step two-electron or two-step single-electron O_2 reduction reaction. The current state of research indicates that the photocatalytic efficiency with sacrificial agents (often alcohols) is much greater than without. Bacterial disinfection relies primarily on the production of strongly oxidizing substances ($\cdot OH$,$\cdot O_2^-$ and H_2O_2) to inactivate bacteria. To summarize, it is not hard to see that the process of activating O_2 plays a crucial role in all these applications, which may be the direction of future efforts to design and develop improved photocatalysts.

5. Conclusions and prospects

In conclusion, g-C_3N_4-based metal-free catalysts are motivating new excitement in future research due to their promise to solve or alleviate the environmental problems and energy crisis. Based on the metal-free nature of g-C_3N_4, in this review, we present the unique structures, attractive properties and emerging applications of various non-metal modified g-C_3N_4, and briefly summarize the latest developments in these fields. As far as the current development status is concerned, we have made great progress in the study of non-metal modified g-C_3N_4, but there are still many challenges and developments.

First of all, to ensure a high catalytic efficiency, most methods of material synthesis require a tightly controlled reaction environment, but this is not applicable to mass production. We need to develop more mild and effective synthesis methods for industrial production at large scale of high-quality g-C_3N_4-based non-metal catalysts. It is also necessary to develop additional modification strategies to improve its catalytic performance, for example, exploring more various forms of g-C_3N_4, looking for more dopants.

Secondly, most studies only reveal the relationship between material structures and experimental results, and a few articles cover the catalytic mechanism, but still do not explain it thoroughly. Further research is needed on more precise reaction principles, for instance, the mechanism of ROS generation and conversion. The development of *in-situ* characterization techniques may help us in further understanding. Further clarification of the catalytic mechanism will greatly heighten the application performance of g-C_3N_4 and expand the broader application areas.

Thirdly, the latest research trends show that g-C_3N_4-based materials in photocatalysis have gradually shifted to these interesting applications, including CO_2 reduction, NO_x purification, H_2O_2 production and bacterial disinfection, which will inevitably lead to a new research boom. Meanwhile, this shift is inevitable, and this review is timely. But, there are still some limitations of g-C_3N_4-based metal-free catalysts for above-mentioned applications. For instance, the difficulty of recycling powdered materials, the need to use sacrificial agents for achieving high efficiency, and the generation of undesirable intermediates from material self-decomposition. The interaction of g-C_3N_4-based materials with ROS might cause potential deactivation of the catalysts or secondary contamination [186]. All these are to be studied in depth.

Fourthly, the rise of computational chemistry has provided theoretical guidance for our experimental studies, allowing us to design catalysts with better performance, as well as providing an important theoretical basis for in-depth studies of the catalytic mechanism. For example, the reusability and stability of the catalysts is an important indicator to assess performance. Loss of active

sites leading to blocked catalytic reaction and pore blockage leading to decreased adsorption performance are important factors affecting the reusability of the material. Proper doping sites, compounding two semiconductors with matched energy levels, these are necessary to design a stable catalyst. The use of theoretical calculations to determine the reactive sites or stable doping sites before designing the catalysts can provide a research idea to enhance the reusability and stability of the materials. Therefore, combining theoretical calculations with experimental studies will certainly open a new door for us in future research.

Fifthly, g-C_3N_4-based metal-free materials are photocatalysts with good prospects for practical applications, but have many inherent shortcomings, such as complicated and difficult recovery process, the loss of catalytic activity of recovered particles. To address these challenges, finding immobilized supports with large specific surface area and favorable particle dispersion is one of the possible solutions, such as films, foams, sponges, aerogels and so on [187–191].

Sixthly, g-C_3N_4-based metal-free materials have been widely used in photocatalysis because of its excellent properties, but now there are also some research results demonstrated that these catalysts have promising prospects in other catalytic fields such as electrocatalysis [192–194], photoelectrocatalysis [195,196], Fenton reaction [197,198] and sulfate-based advanced oxidation processes [199]. For example, *N*-vacancy engineered g-C_3N_4 can achieve a faraday efficiency for CH_4 formation of 44 % with a partial current density of 14.8 mA/cm^2 at − 1.27 V vs reversible hydrogen electrode [200]. In another work, hierarchical B-doped g-C_3N_4 nanoplatelets possessed excellent property in photoelectrochemical water splitting for H_2 production, which was about 2.5-fold greater than that of pristine g-C_3N_4 [201]. Therefore, in the future research, non-metal modified g-C_3N_4-based catalysts can also do some in-depth exploration in other catalytic fields.

Finally, with the continuous development of science and technology, more and more materials with good catalytic properties will emerge. Combining these materials with g-C_3N_4 is bound to stimulate interesting properties, and the challenges that exist now regarding g-C_3N_4-based catalysts must certainly be addressed. To sum up, combined with the current scientific research and the higher requirements for material development by environmental protection, g-C_3N_4-based non-metal materials are bound to shine in the new materials field in the future.

Data availability

No data was used for the research described in the article.

Declaration of Competing Interest

The authors declare that they have no known competing financial interests or personal relationships that could have appeared to influence the work reported in this paper.

Acknowledgements

This study was supported by the Program for the National Natural Science Foundation of China (51909084, 51779090), the Natural Science Foundation of Hunan Province, China (2020JJ5069, 2020JJ3009), Hunan Researcher Award Program (2020RC3025) and the Fundamental Research Funds for the Central Universities (531118010247, 531118040083).

References

[1] S. Cao, J. Low, J. Yu, M. Jaroniec, Adv. Mater. 27 (2015) 2150–2176.
[2] Y. Liu, C. Tang, M. Cheng, M. Chen, S. Chen, L. Lei, Y. Chen, H. Yi, Y. Fu, L. Li, ACS Catal. 11 (2021) 13374–13396.
[3] X. Zou, Y. Zhang, Chem. Soc. Rev. 44 (2015) 5148–5180.
[4] Y. Liu, H. Cheng, M. Cheng, Z. Liu, D. Huang, G. Zhang, B. Shao, Q. Liang, S. Luo, T. Wu, S. Xiao, Chem. Eng. J. 417 (2021).
[5] Y. Liu, D. Huang, M. Cheng, Z. Liu, C. Lai, C. Zhang, C. Zhou, W. Xiong, L. Qin, B. Shao, Q. Liang, Coord. Chem. Rev. 409 (2020).
[6] D.L. Huang, G.X. Zhang, J. Yi, M. Cheng, C. Lai, P. Xu, C. Zhang, Y. Liu, C.Y. Zhou, W.J. Xue, R.Z. Wang, Z.H. Li, S. Chen, Chemosphere 263 (2021).
[7] M.S. Nasir, G. Yang, I. Ayub, S. Wang, L. Wang, X. Wang, W. Yan, S. Peng, S. Ramakarishna, Appl. Catal. B 257 (2019).
[8] G. Mamba, A.K. Mishra, Appl. Catal. B 198 (2016) 347–377.
[9] J. Zhu, P. Xiao, H. Li, S.A.C. Carabineiro, ACS Appl. Mater. Interfaces 6 (2014) 16449–16465.
[10] G. Liao, Y. Gong, L. Zhang, H. Gao, G.-J. Yang, B. Fang, Energy Environ. Sci. 12 (2019) 2080–2147.
[11] C. Prasad, H. Tang, Q. Liu, I. Bahadur, S. Karlapudi, Y. Jiang, Int. J. Hydrogen Energy 45 (2020) 337–379.
[12] A. Naseri, M. Samadi, A. Pourjavadi, A.Z. Moshfegh, S. Ramakrishna, J. Mater. Chem. A 5 (2017) 23406–23433.
[13] R. Malik, V.K. Tomer, Renew. Sustain. Energy Rev. 135 (2021) 110235.
[14] S. Wang, J. Zhang, B. Li, H. Sun, S. Wang, Energy Fuels 35 (2021) 6504–6526.
[15] Y.Q. Cui, X.Q. An, S. Zhang, Q.W. Tang, H.C. Lan, H.J. Liu, J.H. Qu, Water Res. 200 (2021).
[16] D.S. Pattanayak, D. Pal, J. Mishra, C. Thakur, Environmental Science and Pollution Research, (2022).
[17] N.F.F. Moreira, M.J. Sampaio, A.R. Ribeiro, C.G. Silva, J.L. Faria, A.M.T. Silva, Appl. Catal. B 248 (2019) 184–192.
[18] S. Wang, F. He, X. Zhao, J. Zhang, Z. Ao, H. Wu, Y. Yin, L. Shi, X. Xu, C. Zhao, S. Wang, H. Sun, Appl. Catal. B 257 (2019).
[19] Y. Yu, K. Wu, W. Xu, D. Chen, J. Fang, X. Zhu, J. Sun, Y. Liang, X. Hu, R. Li, Z. Fang, J. Hazard. Mater. 404 (2021) 124171.
[20] D. Huang, G. Zhang, J. Yi, M. Cheng, C. Lai, P. Xu, C. Zhang, Y. Liu, C. Zhou, W. Xue, R. Wang, Z. Li, S. Chen, Chemosphere 263 (2021) 127672.
[21] Y. Yang, C. Zhang, D. Huang, G. Zeng, J. Huang, C. Lai, C. Zhou, W. Wang, H. Guo, W. Xue, R. Deng, M. Cheng, W. Xiong, Appl. Catal. B-Environ. 245 (2019) 87–99.
[22] B. Li, C. Lai, L. Qin, C. Chu, M. Zhang, S. Liu, X. Liu, H. Yi, J. He, L. Li, M. Li, L. Chen, J. Colloid Interface Sci. 560 (2020) 701–713.
[23] M. Zhang, C. Lai, B. Li, F. Xu, D. Huang, S. Liu, L. Qin, Y. Fu, X. Liu, H. Yi, Y. Zhang, J. He, L. Chen, Chem. Eng. J. 396 (2020).
[24] X. Huo, H. Yi, Y. Fu, Z. An, L. Qin, X. Liu, B. Li, S. Liu, L. Li, M. Zhang, F. Xu, G. Zeng, C. Lai, Environmental Science-Nano (2021).
[25] F. Xu, C. Lai, M. Zhang, B. Li, S. Liu, M. Chen, L. Li, Y. Xu, L. Qin, Y. Fu, X. Liu, H. Yi, X. Yang, J. Colloid Interface Sci. 601 (2021) 196–208.
[26] Y. Hong, L. Wang, E. Liu, J. Chen, Z. Wang, S. Zhang, X. Lin, X. Duan, J. Shi, Inorg. Chem. Front. 7 (2020) 347–355.
[27] H. Guo, H.-Y. Niu, C. Liang, C.-G. Niu, Y. Liu, N. Tang, Y. Yang, H.-Y. Liu, Y.-Y. Yang, W.-J. Wang, Chem. Eng. J. 401 (2020).
[28] T. Yu, Z. Hu, H. Wang, X. Tan, J. Mater. Sci. 55 (2019) 2118–2128.
[29] V.K. V, D. Avisar, L.P. V, Y. Betzalel, H. Mamane, J Hazard Mater, 398 (2020) 122880.
[30] Y. Wang, S. Zhao, Y. Zhang, J. Fang, W. Chen, S. Yuan, Y. Zhou, ACS Sustainable Chem. Eng. 6 (2018) 10200–10210.
[31] H. Qi, Y. Liu, C. Li, X. Zou, Y. Huang, Y. Wang, Mater. Lett. 264 (2020).
[32] T.-J. Jiang, C.-W. Luo, C. Xie, Y.-H. Wei, A. Li, RSC Adv. 10 (2020) 32906–32918.
[33] C. Lai, N. An, B. Li, M. Zhang, H. Yi, S. Liu, L. Qin, X. Liu, L. Li, Y. Fu, F. Xu, Z. Wang, X. Shi, Z. An, X. Zhou, Chem. Eng. J. 406 (2021).
[34] Y. Duan, L. Deng, Z. Shi, X. Liu, H. Zeng, H. Zhang, J. Crittenden, J. Colloid Interface Sci. 561 (2020) 696–707.
[35] L. Zhang, J. Zhang, Y. Xia, M. Xun, H. Chen, X. Liu, X. Yin, Int. J. Mol. Sci. 21 (2020).
[36] G. Zhang, D. Huang, M. Cheng, L. Lei, S. Chen, R. Wang, W. Xue, Y. Liu, Y. Chen, Z. Li, J. Mater. Chem. A 8 (2020) 17883–17906.
[37] J. Lin, W. Tian, H. Zhang, X. Duan, H. Sun, S. Wang, Energy Fuels 35 (2021) 7–24.
[38] S. Liang, F. Liu, L. Jiang, Curr. Opin. Green Sustainable Chem. 25 (2020) 100361.
[39] L. Zhou, H. Zhang, H. Sun, S. Liu, M.O. Tade, S. Wang, W. Jin, Catal. Sci. Technol. 6 (2016) 7002–7023.
[40] W. Zhang, D. Xu, F. Wang, M. Chen, Nanoscale Advances 3 (2021) 4370–4387.
[41] F. He, Z. Wang, Y. Li, S. Peng, B. Liu, Appl. Catal. B 269 (2020).
[42] W.J. Ong, L.L. Tan, Y.H. Ng, S.T. Yong, S.P. Chai, Chem. Rev. 116 (2016) 7159–7329.
[43] E. Kroke, M. Schwarz, E. Horath-Bordon, P. Kroll, B. Noll, A.D. Norman, New J. Chem. 26 (2002) 508–512.
[44] V. Hasija, P. Raizada, A. Sudhaik, K. Sharma, A. Kumar, P. Singh, S.B. Jonnalagadda, V.K. Thakur, Appl. Mater. Today 15 (2019) 494–524.
[45] N. Thi Kim Anh, P. Thanh-Truc, N.-P. Huy, E.W. Shin, Applied Surface Science, 537 (2021).
[46] J.-P. Zou, L.-C. Wang, J. Luo, Y.-C. Nie, Q.-J. Xing, X.-B. Luo, H.-M. Du, S.-L. Luo, S.L. Suib, Appl. Catal. B 193 (2016) 103–109.
[47] M.A. Khan, S. Mutahir, F. Wang, W. Lei, M. Xia, S. Zhu, J. Hazard. Mater. 367 (2019) 293–303.
[48] Y. Wang, F. He, L. Chen, J. Shang, J. Wang, S. Wang, H. Song, J. Zhang, C. Zhao, S. Wang, H. Sun, Chin. Chem. Lett. 31 (2020) 2668–2672.

[49] Q. Hao, G. Jia, W. Wei, A. Vinu, Y. Wang, H. Arandiyan, B.-J. Ni, Nano Res. 13 (2019) 18–37.
[50] Y. Li, R. Jin, Y. Xing, J. Li, S. Song, X. Liu, M. Li, R. Jin, Adv. Energy Mater. 6 (2016).
[51] N. Tian, Y. Zhang, X. Li, K. Xiao, X. Du, F. Dong, G.I.N. Waterhouse, T. Zhang, H. Huang, Nano Energy 38 (2017) 72–81.
[52] H. Dou, D. Long, S. Zheng, Y. Zhang, Catal. Sci. Technol. 8 (2018) 3599–3609.
[53] J. Ran, T.Y. Ma, G. Gao, X.-W. Du, S.Z. Qiao, Energy Environ. Sci. 8 (2015) 3708–3717.
[54] X. Ma, Y. Lv, J. Xu, Y. Liu, R. Zhang, Y. Zhu, J. Phys. Chem. C 116 (2012) 23485–23493.
[55] I. Choudhuri, S. Kumar, A. Mahata, K.S. Rawat, B. Pathak, Nanoscale 8 (2016) 14117–14126.
[56] B. Meng, W.-Z. Xiao, L.-L. Wang, L. Yue, S. Zhang, H.-Y. Zhang, PCCP 17 (2015) 22136–22143.
[57] S. Wang, M.-R. Chen, S.-B. Shen, C.-H. Cheng, A.-J. Cai, A.-J. Song, X.-L. Lu, G.-S. Gao, M.-Z. Ma, Z.-W. Zhang, X.-Y. Xu, J. Cleaner Prod. 335 (2022) 130375.
[58] J. Fu, K. Liu, K. Jiang, H. Li, P. An, W. Li, N. Zhang, H. Li, X. Xu, H. Zhou, D. Tang, X. Wang, X. Qiu, M. Liu, Adv Sci (Weinh) 6 (2019) 1900796.
[59] X. Cao, J. Shen, X.F. Li, Y. Luo, ACS Appl. Mater. Interfaces 12 (2020) 52741–52748.
[60] W. Wang, H. Zhou, Y. Liu, S. Zhang, Y. Zhang, G. Wang, H. Zhang, H. Zhao, Small 16 (2020) e1906880.
[61] Z.-F. Huang, J. Song, L. Pan, Z. Wang, X. Zhang, J.-J. Zou, W. Mi, X. Zhang, L. Wang, Nano Energy 12 (2015) 646–656.
[62] Y. Gao, Y. Zhu, L. Lyu, Q. Zeng, X. Xing, C. Hu, Environ. Sci. Technol. 52 (2018) 14371–14380.
[63] P. Qiu, C. Xu, H. Chen, F. Jiang, X. Wang, R. Lu, X. Zhang, Appl. Catal. B 206 (2017) 319–327.
[64] B. Zhu, J. Zhang, C. Jiang, B. Cheng, J. Yu, Appl. Catal. B 207 (2017) 27–34.
[65] C. Liu, Y. Zhang, F. Dong, A.H. Reshak, L. Ye, N. Pinna, C. Zeng, T. Zhang, H. Huang, Appl. Catal. B 203 (2017) 465–474.
[66] A. Mishra, A. Mehta, S. Basu, N.P. Shetti, K.R. Reddy, T.M. Aminabhavi, Carbon 149 (2019) 693–721.
[67] M. Ran, J. Li, W. Cui, Y. Li, P. Li, F. Dong, Catal. Sci. Technol. 8 (2018) 3387–3394.
[68] L. Jiang, X. Yuan, G. Zeng, J. Liang, Z. Wu, H. Yu, D. Mo, H. Wang, Z. Xiao, C. Zhou, J. Colloid Interface Sci. 536 (2019) 17–29.
[69] J. Huang, D. Li, R. Li, Q. Zhang, T. Chen, H. Liu, Y. Liu, W. Lv, G. Liu, Chem. Eng. J. 374 (2019) 242–253.
[70] X. Han, C. Yao, A. Yuan, F. Xi, X. Dong, J. Liu, Mater. Res. Bull. 107 (2018) 477–483.
[71] H. Zhang, X. Han, H. Yu, Y. Zou, X. Dong, Sep. Purif. Technol. 226 (2019) 128–137.
[72] C. Hu, W.-Z. Hung, M.-S. Wang, P.-J. Lu, Carbon 127 (2018) 374–383.
[73] Z. Liu, X. Zhang, Z. Jiang, H.-S. Chen, P. Yang, Int. J. Hydrogen Energy 44 (2019) 20042–20055.
[74] C. Muhire, A. Tesfay Reda, D. Zhang, X. Xu, C. Cui, Chem. Eng. J. 431 (2022) 133816.
[75] Q. Liu, J. Shen, X. Yu, X. Yang, W. Liu, J. Yang, H. Tang, H. Xu, H. Li, Y. Li, J. Xu, Appl. Catal. B 248 (2019) 84–94.
[76] X.L. Wang, W.Q. Fang, H.F. Wang, H. Zhang, H. Zhao, Y. Yao, H.G. Yang, J. Mater. Chem. A 1 (2013) 14089–14096.
[77] Z. Liang, G. Ba, H. Li, N. Du, W. Hou, J. Alloy. Compd. 815 (2020) 152488.
[78] N. Nataraj, T.-W. Chen, M. Akilarasan, S.M. Chen, A.A. Al-Ghamdi, M.S. Elshikh, Chemosphere 302 (2022) 134765.
[79] M.A. Mohamed, M.F.M. Zain, L. Jeffery Minggu, M.B. Kassim, N.A. Saidina Amin, W.N.W. Salleh, M.N.I. Salehmin, M.F. Md Nasir, Z.A. Mohd Hir, Appl. Catal. B 236 (2018) 265–279.
[80] Z. Mo, X. Zhu, Z. Jiang, Y. Song, D. Liu, H. Li, X. Yang, Y. She, Y. Lei, S. Yuan, H. Li, L. Song, Q. Yan, H. Xu, Appl. Catal. B 256 (2019) 117854.
[81] K. Qi, N. Cui, M. Zhang, Y. Ma, G. Wang, Z. Zhao, A. Khataee, Chemosphere 272 (2021).
[82] H. Wang, Y. Bian, J. Hu, L. Dai, Appl. Catal. B 238 (2018) 592–598.
[83] P. Wang, C. Guo, S. Hou, X. Zhao, L. Wu, Y. Pei, Y. Zhang, J. Gao, J. Xu, J. Alloy. Compd. 769 (2018) 503–511.
[84] S. Guo, Y. Tang, Y. Xie, C. Tian, Q. Feng, W. Zhou, B. Jiang, Appl. Catal. B 218 (2017) 664–671.
[85] Y. Wang, Y. Di, M. Antonietti, H. Li, X. Chen, X. Wang, Chem. Mater. 22 (2010) 5119–5121.
[86] E.-X. Han, Y.-Y. Li, Q.-H. Wang, W.-Q. Huang, L. Luo, W. Hu, G.-F. Huang, J. Mater. Sci. Technol. 35 (2019) 2288–2296.
[87] M. Wang, Y. Zeng, G. Dong, C. Wang, Chin. J. Catal. 41 (2020) 1498–1510.
[88] Z.-A. Lan, G. Zhang, X. Wang, Appl. Catal. B 192 (2016) 116–125.
[89] W. Iqbal, B. Yang, X. Zhao, M. Rauf, I.M.A. Mohamed, J. Zhang, Y. Mao, Catal. Sci. Technol. 10 (2020) 549–559.
[90] Q. Han, C. Hu, F. Zhao, Z. Zhang, N. Chen, L. Qu, J. Mater. Chem. A 3 (2015) 4612–4619.
[91] L. Jiang, X. Yuan, G. Zeng, X. Chen, Z. Wu, J. Liang, J. Zhang, H. Wang, H. Wang, ACS Sustainable Chem. Eng. 5 (2017) 5831–5841.
[92] X. Song, X. Li, X. Zhang, Y. Wu, C. Ma, P. Huo, Y. Yan, Appl. Catal. B 268 (2020) 118736.
[93] Y. Yang, H. Jin, C. Zhang, H. Gan, F. Yi, H. Wang, J. Alloy. Compd. 821 (2020) 153439.
[94] X. Feng, H. Chen, F. Jiang, X. Wang, J. Colloid Interface Sci. 509 (2018) 298–306.
[95] H. Ma, Y. Li, S. Li, N. Liu, Appl. Surf. Sci. 357 (2015) 131–138.
[96] C. Yang, W. Teng, Y. Song, Y. Cui, Chin. J. Catal. 39 (2018) 1615–1624.
[97] L. Tao, H. Zhang, G. Li, C. Liao, G. Jiang, Sci. Total Environ. 824 (2022) 153845.
[98] S. Li, G. Dong, R. Hailili, L. Yang, Y. Li, F. Wang, Y. Zeng, C. Wang, Appl. Catal. B 190 (2016) 26–35.
[99] J. Tan, N. Tian, Z. Li, J. Li, X. Yao, M. Vakili, Y. Lu, T. Zhang, Chem. Eng. J. 421 (2021).
[100] L. Shi, L. Yang, W. Zhou, Y. Liu, L. Yin, X. Hai, H. Song, J. Ye, Small 14 (2018).
[101] C.-C. Nguyen, T.-O. Do, ACS Appl. Energy Mater. 1 (2018) 4716–4723.
[102] H. Sun, F. Guo, J. Pan, W. Huang, K. Wang, W. Shi, Chem. Eng. J. 406 (2021).
[103] X. Wang, G. Sun, N. Li, P. Chen, Chem. Soc. Rev. 45 (2016) 2239–2262.
[104] H. Liu, M. Cheng, Y. Liu, J. Wang, G. Zhang, L. Li, L. Du, G. Wang, S. Yang, X. Wang, Energy Environ. Sci. (2022).
[105] W. Fu, J. Yi, M. Cheng, Y. Liu, G. Zhang, L. Li, L. Du, B. Li, G. Wang, X. Yang, J. Hazard. Mater. 424 (2022).
[106] Y. Fu, G. Zeng, C. Lai, D. Huang, L. Qin, H. Yi, X. Liu, M. Zhang, B. Li, S. Liu, L. Li, M. Li, W. Wang, Y. Zhang, Z. Pi, Chem. Eng. J. 399 (2020).
[107] H. Zhang, L. Zhao, F. Geng, L.-H. Guo, B. Wan, Y. Yang, Appl. Catal. B 180 (2016) 656–662.
[108] S. Fang, Y. Xia, K. Lv, Q. Li, J. Sun, M. Li, Appl. Catal. B 185 (2016) 225–232.
[109] D. Qu, J. Liu, X. Miao, M. Han, H. Zhang, Z. Cui, S. Sun, Z. Kang, H. Fan, Z. Sun, Appl. Catal. B 227 (2018) 418–424.
[110] S. Tao, T. Feng, C. Zheng, S. Zhu, B. Yang, J. Phys. Chem. Lett. 10 (2019) 5182–5188.
[111] Y. Hong, Y. Meng, G. Zhang, B. Yin, Y. Zhao, W. Shi, C. Li, Sep. Purif. Technol. 171 (2016) 229–237.
[112] J. Liu, H. Xu, Y. Xu, Y. Song, J. Lian, Y. Zhao, L. Wang, L. Huang, H. Ji, H. Li, Appl. Catal. B 207 (2017) 429–437.
[113] H. Li, X. He, Y. Liu, H. Huang, S. Lian, S.-T. Lee, Z. Kang, Carbon 49 (2011) 605–609.
[114] A.B. Bourlinos, G. Trivizas, M.A. Karakassides, M. Baikousi, A. Kouloumpis, D. Gournis, A. Bakandritsos, K. Hola, O. Kozak, R. Zboril, I. Papagiannouli, P. Aloukos, S. Couris, Carbon 83 (2015) 173–179.
[115] F. Wang, P. Chen, Y. Feng, Z. Xie, Y. Liu, Y. Su, Q. Zhang, Y. Wang, K. Yao, W. Lv, G. Liu, Appl. Catal. B 207 (2017) 103–113.
[116] Q. Xu, P. Pu, J. Zhao, C. Dong, C. Gao, Y. Chen, J. Chen, Y. Liu, H. Zhou, J. Mater. Chem. A 3 (2015) 542–546.
[117] J. Zhou, X. Shan, J. Ma, Y. Gu, Z. Qian, J. Chen, H. Feng, RSC Adv. 4 (2014) 5465–5468.
[118] R.X. Seng, L.L. Tan, W.P.C. Lee, W.J. Ong, S.P. Chai, J. Environ. Manage. 255 (2020) 109936.
[119] W. Lei, Y. Mi, R. Feng, P. Liu, S. Hu, J. Yu, X. Liu, J.A. Rodriguez, J.-O. Wang, L. Zheng, K. Tang, S. Zhu, G. Liu, M. Liu, Nano Energy 50 (2018) 552–561.
[120] W. Wang, Q. Niu, G. Zeng, C. Zhang, D. Huang, B. Shao, C. Zhou, Y. Yang, Y. Liu, H. Guo, W. Xiong, L. Lei, S. Liu, H. Yi, S. Chen, X. Tang, Appl. Catal. B 273 (2020).
[121] X. Zhu, T. Zhang, Z. Sun, H. Chen, J. Guan, X. Chen, H. Ji, P. Du, S. Yang, Adv. Mater. 29 (2017).
[122] L. Kong, Y. Ji, Z. Dang, J. Yan, P. Li, Y. Li, S. Liu, Adv. Funct. Mater. 28 (2018).
[123] D. Li, Y. Liu, C. Wen, J. Huang, R. Li, H. Liu, J. Zhong, P. Chen, W. Lv, G. Liu, J. Hazard. Mater. 436 (2022) 129171.
[124] Y. Wang, Y. Li, J. Zhao, J. Wang, Z. Li, Int. J. Hydrogen Energy 44 (2019) 618–628.
[125] L. Zhou, Y. Tian, J. Lei, L. Wang, Y. Liu, J. Zhang, Catal. Sci. Technol. 8 (2018) 2617–2623.
[126] S. Asadzadeh-Khaneghah, A. Habibi-Yangjeh, K. Nakata, J. Photochem. Photobiol., A 374 (2019) 161–172.
[127] W. Wang, Z. Zeng, G. Zeng, C. Zhang, R. Xiao, C. Zhou, W. Xiong, Y. Yang, L. Lei, Y. Liu, D. Huang, M. Cheng, Y. Yang, Y. Fu, H. Luo, Y. Zhou, Chem. Eng. J. 378 (2019) 122132.
[128] C. Xu, Q. Han, Y. Zhao, L. Wang, Y. Li, L. Qu, J. Mater. Chem. A 3 (2015) 1841–1846.
[129] A. Yuan, H. Lei, F. Xi, J. Liu, L. Qin, Z. Chen, X. Dong, J. Colloid Interface Sci. 548 (2019) 56–65.
[130] Z. Mou, C. Lu, K. Yu, H. Wu, H. Zhang, J. Sun, M. Zhu, M. Cynthia Goh, Energy Technology 7 (2019) 1800589.
[131] A. Cai, Q. Wang, Y. Chang, X. Wang, J. Alloy. Compd. 692 (2017) 183–189.
[132] H. Li, G. Huang, H. Xu, Z. Yang, X. Xu, J. Li, A. Qu, Y. Chen, J. Solid State Chem. 292 (2020) 121705.
[133] J.L. Zhao, Y.S. Liu, Y.P. Wang, H.J. Li, J.S. Wang, Z.J. Li, Appl. Surf. Sci. 470 (2019) 923–932.
[134] P. Qiu, C. Xu, N. Zhou, H. Chen, F. Jiang, Appl. Catal. B 221 (2018) 27–35.
[135] J. Hu, C. Chen, T. Hu, J. Li, H. Lu, Y. Zheng, X. Yang, C. Guo, C.M. Li, J. Mater. Chem. A 8 (2020) 19484–19492.
[136] Q. Zhang, S. Huang, J. Deng, D.T. Gangadharan, F. Yang, Z. Xu, G. Giorgi, M. Palummo, M. Chaker, D. Ma, Adv. Funct. Mater. 29 (2019).
[137] X. Wang, J. Meng, X. Yang, A. Hu, Y. Yang, Y. Guo, ACS Appl. Mater. Interfaces 11 (2019) 588–602.
[138] G. Dong, L. Yang, F. Wang, L. Zang, C. Wang, ACS Catal. 6 (2016) 6511–6519.
[139] J. Zhang, X. Zhao, Y. Wang, Y. Gong, D. Cao, M. Qiao, Appl. Catal. B 237 (2018) 976–985.
[140] P. Sun, H. Liu, M. Feng, Z. Zhai, Y. Fang, X. Zhang, V.K. Sharma, Appl. Catal. B 272 (2020).
[141] Y. Zhou, L. Zhang, W. Huang, Q. Kong, X. Fan, M. Wang, J. Shi, Carbon 99 (2016) 111–117.

[142] K.C. Christoforidis, Z. Syrgiannis, V. La Parola, T. Montini, C. Petit, E. Stathatos, R. Godin, J.R. Durrant, M. Prato, P. Fornasiero, Nano Energy 50 (2018) 468–478.
[143] Q. Liu, H. Tian, Z. Dai, H. Sun, J. Liu, Z. Ao, S. Wang, C. Han, S. Liu, Nano-Micro Letters 12 (2020) 24.
[144] W. Wang, G. Li, T. An, D.K.L. Chan, J.C. Yu, P.K. Wong, Appl. Catal. B 238 (2018) 126–135.
[145] X. Zeng, Y. Liu, Y. Xia, M.H. Uddin, D. Xia, D.T. McCarthy, A. Deletic, J. Yu, X. Zhang, Appl. Catal. B 274 (2020).
[146] H. Liu, H. Li, J. Lu, S. Zeng, M. Wang, N. Luo, S. Xu, F. Wang, ACS Catal. 8 (2018) 4761–4771.
[147] Y. Kofuji, S. Ohkita, Y. Shiraishi, H. Sakamoto, S. Tanaka, S. Ichikawa, T. Hirai, ACS Catal. 6 (2016) 7021–7029.
[148] S. Liu, J. Ke, H. Sun, J. Liu, M.O. Tade, S. Wang, Appl. Catal. B 204 (2017) 358–364.
[149] Q. Liu, L. Zhou, J. Gao, S. Wang, L. Liu, S. Liu, J. Colloid Interface Sci. 569 (2020) 12–21.
[150] H. Sun, G. Zhou, Y. Wang, A. Suvorova, S. Wang, ACS Appl. Mater. Interfaces 6 (2014) 16745–16754.
[151] D. He, D. Jin, F. Cheng, T. Zhang, J. Qu, Y. Zhou, X. Yuan, Y.-N. Zhang, W.J.G.M. Peijnenburg, Sci. Total Environ. 804 (2022) 150062.
[152] R. Tang, D. Gong, Y. Zhou, Y. Deng, C. Feng, S. Xiong, Y. Huang, G. Peng, L. Li, Z. Zhou, Appl. Catal. B 303 (2022) 120929.
[153] D. Yuan, W. Huang, X. Chen, Z. Li, J. Ding, L. Wang, H. Wan, W.-L. Dai, G. Guan, Appl. Surf. Sci. 489 (2019) 658–667.
[154] Y. Guo, R. Wang, P. Wang, Y. Li, C. Wang, Chemosphere 179 (2017) 84–91.
[155] K. Venkatesan Savunthari, D. Arunagiri, S. Shanmugam, S. Ganesan, M.V. Arasu, N.A. Al-Dhabi, N.T.L. Chi, V.K. Ponnusamy, Chemosphere 272 (2021) 129801.
[156] Z. Kovacic, B. Likozar, M. Hus, ACS Catal. 10 (2020) 14984–15007.
[157] B. Yang, J. Zhao, W. Yang, X. Sun, R. Wang, X. Jia, J. Colloid Interface Sci. 589 (2021) 179–186.
[158] M. Zahid, D. Zhang, X. Xu, M. Pan, M.H. ul haq, A.T. Reda, W. Xu, J. Hazard. Mater. 416 (2021) 125835.
[159] J. Fu, B. Zhu, C. Jiang, B. Cheng, W. You, J. Yu, Small 13 (2017).
[160] N. Sagara, S. Kamimura, T. Tsubota, T. Ohno, Appl. Catal. B 192 (2016) 193–198.
[161] P. Xia, B. Zhu, J. Yu, S. Cao, M. Jaroniec, J. Mater. Chem. A 5 (2017) 3230–3238.
[162] C. Han, J. Li, Z. Ma, H. Xie, G.I.N. Waterhouse, L. Ye, T. Zhang, Sci. China Mater. 61 (2018) 1159–1166.
[163] Q. Li, S. Wang, Z. Sun, Q. Tang, Y. Liu, L. Wang, H. Wang, Z. Wu, Nano Res. 12 (2019) 2749–2759.
[164] X. Wang, Q. Li, L. Gan, X. Ji, F. Chen, X. Peng, R. Zhang, J. Energy Chem. 53 (2021) 139–146.
[165] J. Li, P. Yan, K. Li, W. Cen, X. Yu, S. Yuan, Y. Chu, Z. Wang, Chin. J. Catal. 39 (2018) 1695–1703.
[166] L. Duan, G. Li, S. Zhang, H. Wang, Y. Zhao, Y. Zhang, Chem. Eng. J. 411 (2021).
[167] G. Dong, D.L. Jacobs, L. Zang, C. Wang, Appl. Catal. B 218 (2017) 515–524.
[168] X. Wang, J. Huang, F. Hu, J. Chen, X. Yao, J. Nanopart. Res. 23 (2021).
[169] S. Samanta, R. Yadav, A. Kumar, A. Kumar Sinha, R. Srivastava, Appl. Catal. B 259 (2019).
[170] L. Zhou, J. Lei, F. Wang, L. Wang, M.R. Hoffmann, Y. Liu, S.-I. In, J. Zhang, Appl. Catal. B 288 (2021).
[171] H. Liu, M. Cheng, Y. Liu, G. Zhang, L. Li, L. Du, B. Li, S. Xiao, G. Wang, X. Yang, Coord. Chem. Rev. 458 (2022).
[172] Y. Shiraishi, Y. Kofuji, H. Sakamoto, S. Tanaka, S. Ichikawa, T. Hirai, ACS Catal. 5 (2015) 3058–3066.
[173] X. Dang, R. Yang, Z. Wang, S. Wu, H. Zhao, J. Mater. Chem. A 8 (2020) 22720–22727.
[174] Z. Wei, M. Liu, Z. Zhang, W. Yao, H. Tan, Y. Zhu, Energy Environ. Sci. 11 (2018) 2581–2589.
[175] C. Feng, L. Tang, Y. Deng, J. Wang, Y. Liu, X. Ouyang, H. Yang, J. Yu, J. Wang, Appl. Catal. B 281 (2021).
[176] S. Zhao, T. Guo, X. Li, T. Xu, B. Yang, X. Zhao, Appl. Catal. B 224 (2018) 725–732.
[177] Z. Zhu, H. Pan, M. Murugananthan, J. Gong, Y. Zhang, Appl. Catal. B 232 (2018) 19–25.
[178] W. Wang, C. Zhou, Y. Yang, G. Zeng, C. Zhang, Y. Zhou, J. Yang, D. Huang, H. Wang, W. Xiong, X. Li, Y. Fu, Z. Wang, Q. He, M. Jia, H. Luo, Chem. Eng. J. 404 (2021).
[179] Q. Shi, S. Deng, Y. Zheng, Y. Du, L. Li, S. Yang, G. Zhang, L. Du, G. Wang, M. Cheng, Y. Liu, Environ. Res. 212 (2022).
[180] N. Ding, X. Chang, N. Shi, X. Yin, F. Qi, Y. Sun, Environ. Sci. Pollut. Res. Int. 26 (2019) 18730–18738.
[181] D. He, Z. Zhang, Y. Xing, Y. Zhou, H. Yang, H. Liu, J. Qu, X. Yuan, J. Guan, Y.-N. Zhang, Chem. Eng. J. 384 (2020).
[182] Z. Teng, N. Yang, H. Lv, S. Wang, M. Hu, C. Wang, D. Wang, G. Wang, Chem 5 (2019) 664–680.
[183] J. Xiao, Q. Liu, M. Song, X. Li, Q. Li, J.K. Shang, Water Res. 198 (2021) 117125.
[184] C. Tang, C. Liu, Y. Han, Q. Guo, W. Ouyang, H. Feng, M. Wang, F. Xu, Adv Healthc Mater 8 (2019) e1801534.
[185] C. Zhang, M. Zhang, Y. Li, D. Shuai, Appl. Catal. B 248 (2019) 11–21.
[186] J. Xiao, Q. Han, Y. Xie, J. Yang, Q. Su, Y. Chen, H. Cao, Environ. Sci. Technol. 51 (2017) 13380–13387.
[187] J. Hu, D. Chen, N. Li, Q. Xu, H. Li, J. He, J. Lu, Small 14 (2018) 1800416.
[188] R. Zhang, A. Zhang, Y. Yang, Y. Cao, F. Dong, Y. Zhou, J. Hazard. Mater. 397 (2020) 122822.
[189] F. Dong, Z. Wang, Y. Li, W.-K. Ho, S.C. Lee, Environ. Sci. Technol. 48 (2014) 10345–10353.
[190] J. Tang, J. Wang, L. Tang, C. Feng, X. Zhu, Y. Yi, H. Feng, J. Yu, X. Ren, Chem. Eng. J. 430 (2022) 132669.
[191] Y. Yang, Q. Zhang, R. Zhang, T. Ran, W. Wan, Y. Zhou, Front. Chem. 6 (2018).
[192] J. Kim, A.P. Tiwari, M. Choi, Q. Chen, J. Lee, T.G. Novak, M. Park, K. Kim, K.-S. An, S. Jeon, J. Mater. Chem. A (2022).
[193] M.A. Wahab, J. Joseph, L. Atanda, U.K. Sultana, J.N. Beltramini, K. Ostrikov, G. Will, A.P. O'Mullane, A. Abdala, ACS Appl. Energy Mater. 3 (2020) 1439–1447.
[194] V.S. Kale, U. Sim, J. Yang, K. Jin, S.I. Chae, W.J. Chang, A.K. Sinha, H. Ha, C.-C. Hwang, J. An, H.-K. Hong, Z. Lee, K.T. Nam, T. Hyeon, Small 13 (2017) 1603893.
[195] F. Liang, Y. Zhu, Appl. Catal. B 180 (2016) 324–329.
[196] S. Tian, C. Dang, R. Mao, X. Zhao, ACS Sustainable Chem. Eng. 6 (2018) 10273–10281.
[197] W.L. Oliveira, M.A. Ferreira, H.A.J.L. Mourão, M.J.M. Pires, V. Ferreira, H.F. Gorgulho, D.F. Cipriano, J.C.C. Freitas, V.R. Mastelaro, O.R. Nascimento, D.E.C. Ferreira, F. Ramos Fioravante, M.C. Pereira, J.P. de Mesquita, J. Colloid Interface Sci. 587 (2021) 479–488.
[198] Z. Liu, Q. Shen, C. Zhou, L. Fang, M. Yang, T. Xia, Catalysts 8 (2018).
[199] K.-Y.-A. Lin, Z.-Y. Zhang, T. Wi-Afedzi, J. Water Process Eng. 24 (2018) 83–89.
[200] Z. Chen, M.-R. Gao, Y.-Q. Zhang, N. Duan, T. Fan, J. Xiao, J. Zhang, Y. Dong, J. Li, X. Yi, J.-L. Luo, Nano Energy 73 (2020) 104833.
[201] Y. Ding, S. Maitra, C. Wang, R. Zheng, M. Zhang, T. Barakat, S. Roy, J. Liu, Y. Li, T. Hasan, B.-L. Su, Journal of Energy Chemistry 70 (2022) 236–247.